CHAPTER 4

The Radon-Wigner Transform in Analysis, Design, and Processing of Optical Signals

Walter D. Furlan and Genaro Saavedra

Universitat de València, Optics Department
Burjassot, Spain

4.1 Introduction

One of the main features of phase space is that its conjugate coordinates are noncommutative and cannot be simultaneously specified with absolute accuracy. As a consequence, there is no phase-space joint distribution that can be formally interpreted as a joint probability density. Indeed, most of the classic phase-space distributions, such as the Wigner distribution function (WDF), the ambiguity function (AF), or the complex spectrogram, have difficult interpretation problems due to the complex, or negative, values they have in general. Besides, they may be nonzero even in regions of the phase space where either the signal or its Fourier transform vanishes. This is a critical issue, especially for the characterization of nonstationary or nonperiodic signals. As an alternative, the projections (*marginals*) of the phase-space distributions are strictly positive, and as we will see below, they give information about the signal on both phase-space variables. These projections can be formally associated with probability functions, avoiding all interpretation ambiguities associated with the original phase-space distributions. This is the case of the Radon-Wigner transform (RWT), closely related to the projections of the WDF in phase space and also intimately connected with AF, as will be shown.

The general structure of this chapter is as follows. In Sec. 4.2, a general overview of mathematical properties of the RWT is given, and a summary of different optical setups for achieving it is presented. Next, the use of this representation in the analysis of optical signals and systems is developed in several aspects, namely, the computation of diffraction intensities, the optical display of Fresnel patterns, the amplitude and phase reconstruction of optical fields, and the calculation of merit function in imaging systems. Finally, in Sec. 4.4, a review of design techniques, based on the utilization of the RWT, for these imaging systems is presented, along with some techniques for optical signal processing.

4.2 Projections of the Wigner Distribution Function in Phase Space: The Radon-Wigner Transform (RWT)

The RWT was first introduced for the analysis and synthesis of frequency-modulated time signals, and it is a relatively new formalism in optics.[1,2] However, it has found several applications in this field during the last years. Many of them, such as the analysis of diffraction patterns, the computation of merit functions of optical systems, or the tomographic reconstruction of optical fields, are discussed in this chapter. We start by presenting the definition and some basic properties of the RWT. The optical implementation of the RWT which is the basis for many of the applications is discussed next.

Note, as a general remark, that for the sake of simplicity most of the formal definitions for the signals used hereafter are restricted to one-dimensional signals, i.e., functions of a single variable $f(x)$. This is mainly justified by the specific use of these properties that we present in this chapter. The generalization to more than one variable is in most cases straightforward. We will refer to the dual variables x and ξ as *spatial* and *spatial-frequency* coordinates, since we will deal mainly with signals varying on space. Of course, if the signal is a function of time instead of space, the terms *time* and *frequency* should be applied.

4.2.1 Definition and Basic Properties

We start this section by recalling the definition of the WDF associated with a complex function $f(x)$, namely,

$$\begin{aligned}\mathcal{W}\{f(x'), x, \xi\} &= W_f(x, \xi)\\ &= \int_{-\infty}^{+\infty} f\left(x+\frac{x'}{2}\right) f^*\left(x-\frac{x'}{2}\right) \exp\left(-i2\pi\xi x'\right) dx' \end{aligned} \tag{4.1}$$

which also can be defined in terms of the Fourier transform (FT) of the original signal

$$\mathcal{F}\{f(x), \xi\} = F(\xi) = \int_{-\infty}^{+\infty} f(x) \exp(-i2\pi\xi x)\, dx \tag{4.2}$$

as

$$W_f(x, \xi) = \int_{-\infty}^{+\infty} F\left(\xi + \frac{\xi'}{2}\right) F^*\left(\xi - \frac{\xi'}{2}\right) \exp(i2\pi\xi' x)\, d\xi' \tag{4.3}$$

It is interesting to remember that any WDF can be inverted to recover, up to a phase constant, the original signal or, equivalently, its Fourier transform. The corresponding inversion formulas are[3]

$$f(x) = \frac{1}{f^*(x')} \int_{-\infty}^{+\infty} W_f\left(\frac{x + x'}{2}, \xi\right) \exp[i2\pi\xi(x - x')]\, d\xi \tag{4.4}$$

$$F(\xi) = \frac{1}{F^*(\xi')} \int_{-\infty}^{+\infty} W_f\left(x, \frac{\xi + \xi'}{2}\right) \exp[-i2\pi(\xi - \xi')x]\, dx \tag{4.5}$$

Note that these equations state the uniqueness of the relationship between the signal and the corresponding WDF (except for a phase constant). It is straightforward to deduce from these formulas that the integration of the WDF on the spatial or spatial-frequency coordinate leads to the modulus square of the signal or its Fourier transform, respectively, i.e.,

$$|f(x)|^2 = \int_{-\infty}^{+\infty} W_f(x, \xi)\, d\xi \tag{4.6}$$

$$|F(\xi)|^2 = \int_{-\infty}^{+\infty} W_f(x, \xi)\, dx \tag{4.7}$$

These integrals, or *marginals*, can be viewed as the projection of the function $W_f(x, \xi)$ in phase space along straight lines parallel to the ξ axis [in Eq. (4.6)] or to the x axis [in Eq. (4.7)]. These cases are particular ones of all possible projections along straight lines of a given function in phase space. In fact, for any function of (at least) two coordinates,

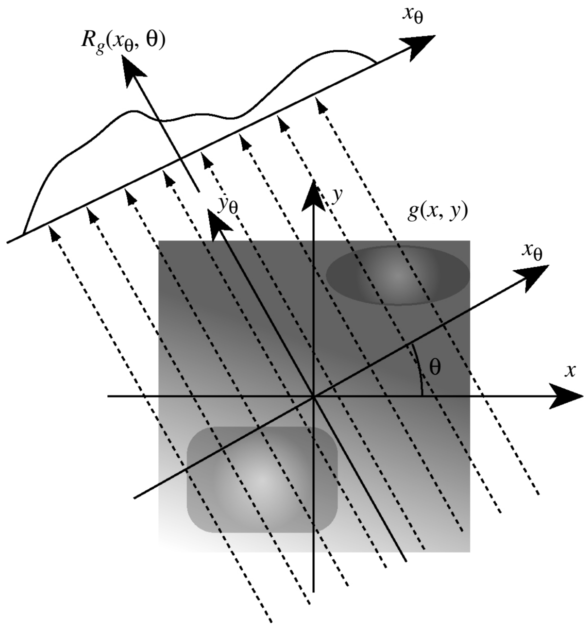

FIGURE 4.1 Projection scheme for the definition of the Radon transform.

say, $g(x, y)$, its Radon transform is defined as a generalized marginal

$$\mathcal{R}\{g(x, y), x_\theta, \theta\} = R_g(x_\theta, \theta) = \int_{-\infty}^{+\infty} g(x, y)\, dy_\theta \tag{4.8}$$

where, as presented in Fig. 4.1, x_θ and y_θ are the coordinates rotated by an angle θ. It is easy to see from this figure that

$$R_g(x_\theta, \theta + \pi) = R_g(-x_\theta, \theta) \tag{4.9}$$

Thus, the reduced domain $\theta \in [0, \pi)$ is used for $R_g(x_\theta, \theta)$. Note that the integration in the above definition is performed along straight lines characterized, for a given pair (x_θ, θ), by the equation

$$\begin{aligned} y &= \frac{x_\theta}{\sin\theta} - \frac{x}{\tan\theta} && \text{for } \theta \neq 0, \frac{\pi}{2} \\ x &= x_\theta && \text{for } \theta = 0 \\ y &= x_\theta && \text{for } \theta = \frac{\pi}{2} \end{aligned} \tag{4.10}$$

and therefore Eq. (4.8) can be reformulated as

$$R_g(x_\theta,\theta)=\begin{cases}\displaystyle\int_{-\infty}^{+\infty} g\left(x,\frac{x_\theta}{\sin\theta}-\frac{x}{\tan\theta}\right)dx & \text{for } \theta\neq 0,\frac{\pi}{2}\\ \displaystyle\int_{-\infty}^{+\infty} g(x_\theta,y)\,dy & \text{for } \theta=0\\ \displaystyle\int_{-\infty}^{+\infty} g(x,x_\theta)\,dx & \text{for } \theta=\frac{\pi}{2}\end{cases}\tag{4.11}$$

Thus, when we consider as projected function $W_f(x,\xi)$, we can define the *generalized marginals* as the Radon transform of this WDF, namely,

$$\begin{aligned}\mathcal{R}\{W_f(x,\xi),x_\theta,\theta\}&=R_{W_f}(x_\theta,\theta)=\int_{-\infty}^{+\infty} W_f(x,\xi)\,d\xi_\theta\\ &=\int_{-\infty}^{+\infty} W_f(x_\theta\cos\theta-\xi\sin\theta,\,x_\theta\sin\theta+\xi\cos\theta)\,d\xi\\ &=\begin{cases}\displaystyle\int_{-\infty}^{+\infty} W_f\left(x,\frac{x_\theta}{\sin\theta}-\frac{x}{\tan\theta}\right)dx & \text{for } \theta\neq 0,\frac{\pi}{2}\\ \displaystyle\int_{-\infty}^{+\infty} W_f(x_\theta,\xi)\,d\xi & \text{for } \theta=0\\ \displaystyle\int_{-\infty}^{+\infty} W_f(x,x_\theta)\,dx & \text{for } \theta=\frac{\pi}{2}\end{cases}\end{aligned}\tag{4.12}$$

where, in the last expression, we have explicitly considered the equations for the integration lines in the projection. In terms of the original signal, this transform is called its Radon-Wigner transform. It is easy to show that

$$\begin{aligned}R_{W_f}(x_\theta,\theta)=RW_f(x_\theta,\theta)&=\int_{-\infty}^{+\infty}\int_{-\infty}^{+\infty} f\left(x_\theta\cos\theta-\xi\sin\theta+\frac{x'}{2}\right)\\ &\times f^*\left(x_\theta\cos\theta-\xi\sin\theta-\frac{x'}{2}\right)\\ &\times\exp[-i2\pi(x_\theta\sin\theta+\xi\cos\theta)x']\,dx'd\xi\end{aligned}\tag{4.13}$$

By performing a proper change in the integration variables, the following more compact expression can be obtained

$$RW_f(x_\theta, \theta) = \begin{cases} \left|\frac{1}{\sin\theta}\right| \left| \int\limits_{-\infty}^{+\infty} f(x) \exp\left(i\pi \frac{x^2}{\tan\theta}\right) \exp\left(-i2\pi \frac{x_\theta x}{\sin\theta}\right) dx \right|^2 & \text{for } \theta \neq 0, \frac{\pi}{2} \\ |f(x_0 = x)|^2 & \text{for } \theta = 0 \\ \left|F\left(x_{\pi/2} = \xi\right)\right|^2 & \text{for } \theta = \frac{\pi}{2} \end{cases} \tag{4.14}$$

From this equation it is clear that

$$RW_f(x_\theta, \theta) \geq 0 \tag{4.15}$$

This is a very interesting property, since the WDF cannot be positive in whole phase space (except for the particular case of a Gaussian signal). Note also that from Eq. (4.14) a symmetry condition can be stated, namely,

$$RW_f(x_\theta, \pi - \theta) = RW_{f^*}(-x_\theta, \theta) \tag{4.16}$$

so that for real signals, that is, $f(x) = f^*(x) \forall x \in \mathbb{R}$, one finds

$$RW_f(x_\theta, \pi - \theta) = RW_f(-x_\theta, \theta) \tag{4.17}$$

and, therefore, for this kind of signal the reduced domain $\theta \in [0, \pi)$ in the Radon transform is clearly redundant. In this case, the range $\theta \in [0, \pi/2]$ contains in fact all the necessary values for a full definition of the RWT.

Equation (4.14) also allows one to link the RWT with another integral transform defined directly from the original signal, namely, the fractional Fourier transform (FrFT). This transformation, often considered a generalization of the classic Fourier transform, is given by

$$\mathcal{F}^p\{f(x), \alpha\} = F_p(\alpha) = \begin{cases} \frac{\exp\left[i\left(\theta + \pi\alpha^2/\tan\theta\right)\right]}{\sqrt{i\sin\theta}} \int\limits_{-\infty}^{+\infty} f(x) \\ \quad \times \exp\left(i\pi\frac{x^2}{\tan\theta}\right) \exp\left(-i2\pi\frac{\alpha x}{\sin\theta}\right) dx & \text{for } \theta \neq 0, \frac{\pi}{2} \\ f(\alpha) & \text{for } \theta = 0 \\ F(\alpha) & \text{for } \theta = \frac{\pi}{2} \end{cases} \tag{4.18}$$

where $\theta = p\pi/2$. From this definition, it is easy to see that

$$RW_f(x_\theta, \theta) = |F_{2\theta/\pi}(x_\theta)|^2 \tag{4.19}$$

so that the RWT can be also interpreted as a two-dimensional representation of all the FrFTs of the original function.

Another interesting relationship can be established between the RWT and the AF associated with the input signal. For our input signal the AF is defined as

$$\begin{aligned}\mathcal{A}\{f(x), \xi', x'\} &= A_f(\xi', x')\\ &= \int_{-\infty}^{+\infty} f\left(x + \frac{x'}{2}\right) f^*\left(x - \frac{x'}{2}\right) \exp(-i2\pi\xi' x)\, dx\end{aligned} \tag{4.20}$$

which can be understood as the two-dimensional FT of the WDF, i.e.,

$$\begin{aligned}\mathcal{F}_{2\mathrm{D}}\{W_f(x, \xi), \xi', x'\} &= \int_{-\infty}^{+\infty}\int_{-\infty}^{+\infty} W_f(x, \xi) \exp\left[-i2\pi(\xi' x + x'\xi)\right] dx\, d\xi\\ &= A_f(\xi', -x')\end{aligned} \tag{4.21}$$

There is a well-known relationship between the two-dimensional FT of a function and the one-dimensional Fourier transformation of its projections. This link is established through the *central slice theorem*, which states that the values of the one-dimensional FT of a projection at an angle θ give a central profile—or *slice*—of the two-dimensional FT of the original signal at the same angle. If we apply this theorem to the WDF, it is straightforward to show that

$$\mathcal{F}\{RW_f(x_\theta, \theta), \xi_\theta\} = A_f(\xi_\theta \cos\theta, -\xi_\theta \sin\theta) \tag{4.22}$$

i.e., the one-dimensional FT of the RWT for a fixed projection angle θ provides a central profile of the AF $A_f(\xi', x')$ along a straight line forming an angle $-\theta$ with the ξ' axis. These relationships together with other links between representations in the phase space are summarized in Fig. 4.2.

To conclude this section, we consider the relationship between the RWT of an input one-dimensional signal $f(x)$ and the RWT of the same signal but after passing through a first-order optical system. In this case, the input signal undergoes a canonical transformation defined through four real parameters (a, b, c, d) or, equivalently, by a 2×2 real matrix

$$M = \begin{pmatrix} a & b \\ c & d \end{pmatrix} \tag{4.23}$$

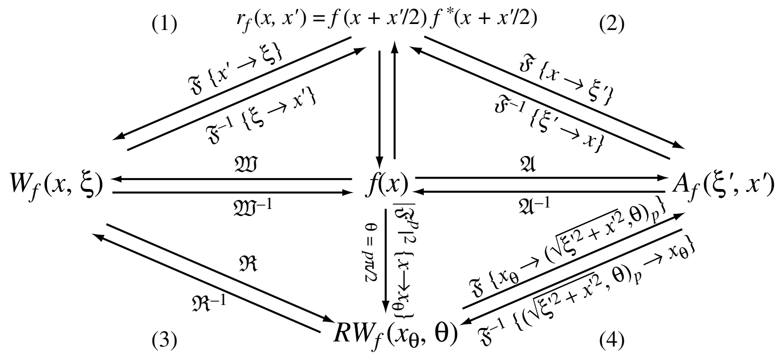

FIGURE 4.2 Relationship diagram between the original signal $f(x)$ and different phase-space representations. $\mathcal{F}$, $\mathcal{F}^p$, $\mathcal{W}$, $\mathcal{A}$, and $\mathcal{R}$ stand for FT, FrFT, WDF integral, AF transform and Radon transformation, respectively, while -1 represents the corresponding inverse operator. (1) WDF and inverse transform; (2) AF and inverse transform; (3) projection (Radon) transformation and tomographic reconstruction operator; (4) expression of the *central slice theorem* applied to Radon transform and AF; and $(\rho, \theta)_p$ represents polar coordinates in phase space.

in such a way that the transformed signal $g(x)$ is given by

$$g(x) = \begin{cases} \frac{1}{\sqrt{ib}} \exp\left(\frac{-i\pi d x'^2}{b}\right) \int\limits_{-\infty}^{+\infty} f(x') \exp\left(\frac{-i\pi a x'^2}{b}\right) \exp\left(\frac{i2\pi}{b} x\, x'\right) dx' & b \neq 0 \\ \exp\left(\frac{-i\pi c x'^2}{a}\right) \frac{1}{\sqrt{a}} f\left(\frac{x}{a}\right) & b = 0 \end{cases} \tag{4.24}$$

which are the one-dimensional counterparts of Eqs. (3.4) and (3.7). We are restricting our attention to nonabsorbing systems corresponding to the condition $\det M = ad - bc = 1$.

The application of a canonical transformation on the signal produces a distortion on the corresponding WDF according to the general law

$$W_g(x, \xi) = W_f(ax + b\xi, cx + d\xi) = W_f(x', \xi') \tag{4.25}$$

where the mapped coordinates are given by

$$\begin{pmatrix} x' \\ \xi' \end{pmatrix} = \begin{pmatrix} a & b \\ c & d \end{pmatrix} \begin{pmatrix} x \\ \xi \end{pmatrix} \tag{4.26}$$

By applying the definition in Eq. (4.12), it is straightforward to obtain

$$RW_g(x_\theta,\theta)=\begin{cases}\int_{-\infty}^{+\infty} W_g\left(x,\frac{x_\theta}{\sin\theta}-\frac{x}{\tan\theta}\right)dx & \text{for } \theta\neq 0,\frac{\pi}{2}\\ \int_{-\infty}^{+\infty} W_g(x_\theta,\xi)\,d\xi & \text{for } \theta=0\\ \int_{-\infty}^{+\infty} W_g(x,x_\theta)\,dx & \text{for } \theta=\frac{\pi}{2}\end{cases}$$

$$=\left\{\begin{array}{ll}\int_{-\infty}^{+\infty} W_f\left(ax+b\left(\frac{x_\theta}{\sin\theta}-\frac{x}{\tan\theta}\right),cx\right. & \\ \qquad \left.+d\left(\frac{x_\theta}{\sin\theta}-\frac{x}{\tan\theta}\right)\right)dx & \text{for } \theta\neq 0,\frac{\pi}{2}\\ \int_{-\infty}^{+\infty} W_f(ax_\theta+b\xi,cx_\theta+d\xi)\,d\xi & \text{for } \theta=0\\ \int_{-\infty}^{+\infty} W_f(ax+bx_\theta,cx+dx_\theta)\,dx & \text{for } \theta=\frac{\pi}{2}\end{array}\right\}$$

$$\propto RW_f(x_{\theta'},\theta') \tag{4.27}$$

where the mapped coordinates for the original RWT are given by

$$\tan\theta'=-\frac{a\tan\theta-b}{c\tan\theta-d},\qquad x_{\theta'}=\frac{x_\theta}{a\sin\theta-b\cos\theta}\sin\theta' \tag{4.28}$$

Let us consider in the following examples a spatially coherent light distribution $f(x)$, with wavelength λ, that travels along a system that imposes a transformation in the input characterized by an *abcd* transform. Special attention is usually paid to the cases $\theta=0,\pi/2$ since, according to Eqs. (4.6) and (4.7), the modulus squared of the *abcd* transform in Eq. (4.24) and its FT are then obtained, respectively.

1. Coherent propagation through a (cylindrical) thin lens. In this case the associated M matrix for the transformation of the light field is given by

$$M_L=\begin{pmatrix}1 & 0\\ \frac{1}{\lambda f} & 1\end{pmatrix} \tag{4.29}$$

with f being the focal length of the lens. Thus, the RWT for the transformed amplitude light distribution is given in this case by

$$RW_g(x_\theta,\theta)\propto RW_f\left(x_{\theta'},\theta'\right),\quad \tan\theta'=-\lambda f\frac{\tan\theta}{\tan\theta-\lambda f},$$
$$x_{\theta'}=\frac{x_\theta}{\sin\theta}\sin\theta' \tag{4.30}$$

A careful calculation for the case of $\theta = 0$ leads to

$$RW_g(x_0, 0) = |g(x_0)|^2 \propto RW_f\,(x_0, 0) \tag{4.31}$$

while for the value $\theta = \pi/2$ the following result is obtained

$$RW_g\left(x_{\pi/2}, \frac{\pi}{2}\right) \propto RW_f\left(x_{\pi/2}\sin\theta', \theta'\right), \qquad \tan\theta' = -\lambda f \tag{4.32}$$

Note that the effect of this propagation through a thin lens of focal length f is also physically equivalent to the illumination of the incident light distribution by a spherical wavefront whose focus is located at a distance $\eta = f$ from the input plane. Thus, the same results discussed here can be applied straightforwardly to that case.

2. Free-space (Fresnel) propagation. If we consider now the Fresnel approximation for the propagation of a transverse coherent light distribution $f(x)$ by a distance z, namely,

$$g\,(x) = \int_{-\infty}^{+\infty} f(x')\exp\left[\frac{i\pi}{\lambda z}(x'-x)^2\right]dx' \tag{4.33}$$

the transformation matrix M is given by

$$M_F = \begin{pmatrix} 1 & -\lambda z \\ 0 & 1 \end{pmatrix} \tag{4.34}$$

and, therefore, the transformed RWT can be calculated through the expression

$$\begin{aligned} RW_g(x_\theta, \theta) &\propto RW_f(x_{\theta'}, \theta'), \qquad \tan\theta' = \tan\theta - \lambda z, \\ x_{\theta'} &= \frac{x_\theta}{\sin\theta + \lambda z\cos\theta}\sin\theta' \end{aligned} \tag{4.35}$$

For the projection with $\theta = 0$, one obtains

$$\begin{aligned} RW_g(x_0, 0) &= |g(x_0)|^2 \propto RW_f(x_{\theta'}, \theta'), \qquad \tan\theta' = -\lambda z, \\ x_{\theta'} &= \frac{x_0}{\lambda z}\sin\theta' \end{aligned} \tag{4.36}$$

and for the orthogonal projection $\theta = \pi/2$ the following result is achieved

$$RW_g\left(x_{\pi/2}, \frac{\pi}{2}\right) \propto RW_f\left(x_{\pi/2}, \frac{\pi}{2}\right) \tag{4.37}$$

3. Magnifier. If a uniform scale factor m is applied to the input function, the associated M matrix is given by

$$M_m = \begin{pmatrix} \frac{1}{m} & 0 \\ 0 & m \end{pmatrix} \tag{4.38}$$

In this case, the RWT is transformed according to the law

$$RW_g(x_\theta, \theta) \propto RW_f(x_{\theta'}, \theta'), \qquad \tan\theta' = \frac{1}{m^2}\tan\theta,$$
$$x_{\theta'} = \frac{m x_\theta}{\sin\theta}\sin\theta' \tag{4.39}$$

The vertical and horizontal projections are given here simply by the following formulas.

$$\begin{aligned} RW_g(x_0, 0) &= |g(x_0)|^2 \propto RW_f\left(\frac{x_0}{m}, 0\right) \\ RW_g\left(x_{\pi/2}, \frac{\pi}{2}\right) &\propto RW_f\left(m x_{\pi/2}, \frac{\pi}{2}\right) \end{aligned} \tag{4.40}$$

4.2.2 Optical Implementation of the RWT: The Radon-Wigner Display

Like any other phase-space function, the RWT also enables an optical implementation that is desirable for applications in the analysis and processing of optical signals. The correct field identification requires a large number of Wigner distribution projections, which raises the necessity to design flexible optical setups to obtain them. The relationship between the RWT and the FrFT, expressed mathematically by Eq. (4.19), suggests that the optical computation of the RWT is possible directly from the input function, omitting the passage through its WDF. In fact, the RWT for a given projection angle is simply the intensity registered at the output plane of a given FrFT transformer. For one-dimensional signals, the RWT for all possible projection angles simultaneously displays a continuous representation of the FrFT of a signal as a function of the fractional Fourier order p, and it is known as the *Radon-Wigner display* (RWD). This representation, proposed by Wood and Barry for its application to the detection and classification of linear FM components,[1] has found several applications in optics as we will see later in this chapter.

Different and simple optical setups have been suggested to implement the FrFT, and most have been the basis for designing other systems to obtain the RWD. The first one described in the literature, designed to obtain the RWD of one-dimensional signals, was proposed by Mendlovic et al.[4] It is based on Lohmann's bulk optics systems for obtaining the FrFT.[5] In this method, the one-dimensional input function is converted to a two-dimensional object by the use of cylindrical lenses to allow the construction of a multichannel processor that optically implements the calculations of the RWD. The setup consists of three phase masks separated by fixed distances in free space. The masks consist of many strips, each one representing a different channel that performs an FrFT with a different order over the input signal. Each strip is a Fresnel zone plate with a different focal length that is selected for obtaining the different fractional order p. Thus, the main shortcoming of the RWD chart produced by this setup is that it has a limited number of projection angles (or fractional orders). Besides the very poor angular resolution, the experimental results obtained in the original paper are actually very far from the theoretical predictions.

A truly continuous display, i.e., a complete RWD setup, was proposed by Granieri et al.[6] This approach is based on the relationship between the FrFT and Fresnel diffraction,[7,8] which establishes that every Fresnel diffraction pattern of an input object is univocally related to a scaled version of a certain FrFT of the same input. Therefore, if the input function $f(x)$ is registered in a transparency with amplitude transmittance $t(x/s)$, with s being the construction scale parameter, then the FrFT of the input can be optically obtained by free-space propagation of a spherical wavefront impinging on it. Actually, the Fresnel diffraction field $U(x, R_p)$ obtained at distance R_p from the input, which is illuminated with a spherical wavefront of radius z and wavelength λ, is related to the FrFT of order p of the input function $\mathcal{F}^p\{t(x), \alpha\}$ as follows.[9]

$$U(x, R_p) = \exp\left\{\frac{i\pi x^2}{\lambda}\left[\frac{z(1-M_p)-R_p}{z\,R_p\,M_p^2}\right]\right\}\mathcal{F}^p\left\{t\left(\frac{x'}{M_p}\right), x\right\} \tag{4.41}$$

where M_p is the magnification of the optical FrFT. For each fractional order, the values of M_p and R_p are related to the system parameters s, λ, and z through

$$R_p = \frac{s^2\lambda^{-1}\tan(p\pi/2)}{1+s^2(z\lambda)^{-1}\tan(p\pi/2)}, \tag{4.42}$$

$$M_p = \frac{1+\tan(p\pi/2)\quad\tan(p\pi/4)}{1+s^2(z\lambda)^{-1}\tan(p\pi/2)} \tag{4.43}$$

These last equations allow us to recognize that by illumination of an input transparency with a spherical wavefront converging to an axial point S, all the FrFTs in the range [0, 1] can be obtained simultaneously, apart from a quadratic-phase factor and a scale factor. The FrFTs are axially distributed between the input transparency plane ($p = 0$) and the virtual source (S) plane ($p = 1$) in which the optical FT of the input is obtained. For one-dimensional input signals, instead of a spherical

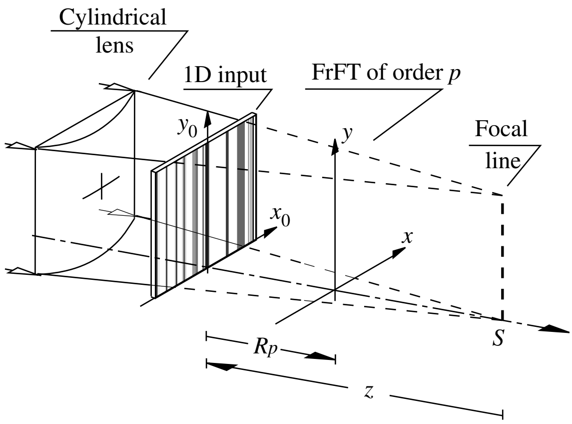

FIGURE 4.3 Implementation of the FrFT by free-space propagation.

wavefront, we can use a cylindrical one to illuminate the input (see Fig. 4.3).

Keeping in mind Eq. (4.19), we see the next step is to obtain the RWD from this setup. To do this, we have to find an optical element to form the image of the axially distributed FrFT channels, at the same output plane simultaneously. Therefore, the focal length of this lens should be different for each fractional order p. Since in this case the different axially located FrFTs present no variations along the vertical coordinate, we can select a different one-dimensional horizontal slice of each one and use it as a single and independent fractional-order channel. (see Fig. 4.4).

The setup of Fig. 4.4 takes advantage of the one-dimensional nature of the input, and it behaves as a multichannel parallel FrFT transformer, provided that the focal length of the lens L varies with the y coordinate in the same way as it varies with p. In this way, the problem can be addressed as follows. For each value of p (vertical coordinate y) we want to image a different object plane at a distance a_p from the lens onto a fixed output plane located at a' from the lens. To obtain this result, it is straightforward to deduce from the Gaussian lens equation and from the distances in Fig. 4.4 that it is necessary to design a lens with a focal length that varies with p (vertical coordinate y) according to

$$f(p) = \frac{a' a_p}{a' + a_p} = \frac{a' l + (1 + l z^{-1}) a' s^2 \lambda^{-1} \tan(p\pi/2)}{a' - l - (a' + l + z) z^{-1} s^2 \lambda^{-1} \tan(p\pi/2)} \qquad (4.44)$$

On the other hand, this focal length should provide the exact magnification at each output channel. The magnification given by the system

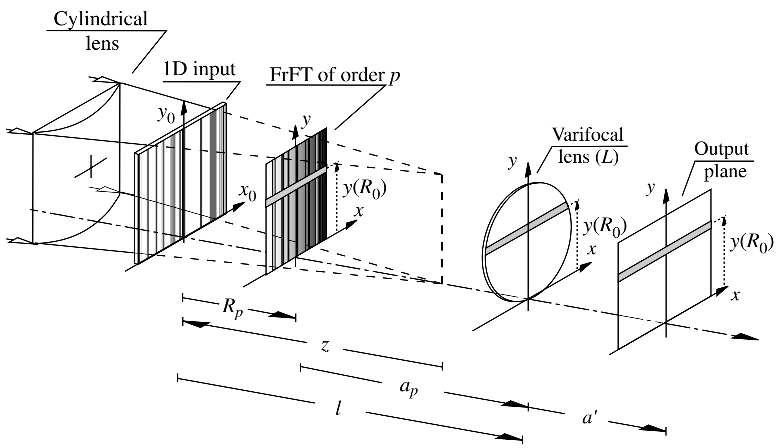

FIGURE 4.4 RWD setup (multichannel continuous FrFT transformer).

for each fractional order p is

$$M_L(p) = \frac{-a'}{a_p} = \frac{a'}{\frac{s^2\lambda^{-1}\tan(p\pi/2)}{1+s^2(z\lambda)^{-1}\tan(p\pi/2)} - l} \tag{4.45}$$

However, for the p-order slice of the RWT of the input function to be achieved, the lens L should counterbalance the magnification of the FRT located at R_p to restore its proper magnification at the output plane. Therefore, by using Eq. (4.43), the magnification provided by L should be

$$M_L(p) = \frac{-1}{M_p} = -\frac{1 + s^2(z\lambda)^{-1}\tan(p\pi/2)}{1 + \tan(p\pi/2) \quad \tan(p\pi/4)} \tag{4.46}$$

Comparing Eqs. (4.45) and (4.46), we note that the functional dependence of both equations on p is different, and, consequently, we are unable to obtain an exact solution for all fractional orders. However, an approximate solution can be obtained by choosing the parameters of the system, namely, s, z, l, λ, and a', in such a way that they minimize the difference between these functions in the interval $p \in [0, 1]$. One way to find the optimum values for these parameters is by a least-squares method. This optimization[6] leads to the following constraint conditions

$$a' = l\left(\frac{1}{2} + \frac{\pi}{4}\right), \qquad z = \frac{-ls^2}{\lambda l + s^2} \tag{4.47}$$

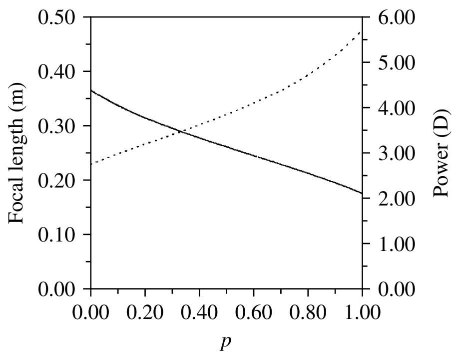

FIGURE 4.5 Focal length (solid curve) and optical power (dotted curve) of the designed varifocal lens L for the values $z = 426$ mm, $l = 646$ mm, and $a = 831$ mm.

The variation of the focal distance of the lens L with p according to Eq. (4.44) and its optical power, under the constraints given by Eqs. (4.47), are represented in Fig. 4.5 for the following values: $z = 426$ mm, $l = 646$ mm, and $a = 831$ mm.

For this particular combination of parameters, the optical power is nearly linear with p, except for values close to $p = 1$. This linearity is also accomplished by some designs of ophthalmic progressive addition lenses in which there is a continuous linear transition between two optical powers that correspond to the *near portion* and *distance portion*. In the experimental verification of the system, a progressive lens of +2.75 D spherical power and +3 D of addition was used in the setup of Fig. 4.4 with the above-mentioned values for the parameters z, l, and a. Figure 4.6 illustrates a comparison between the numerical

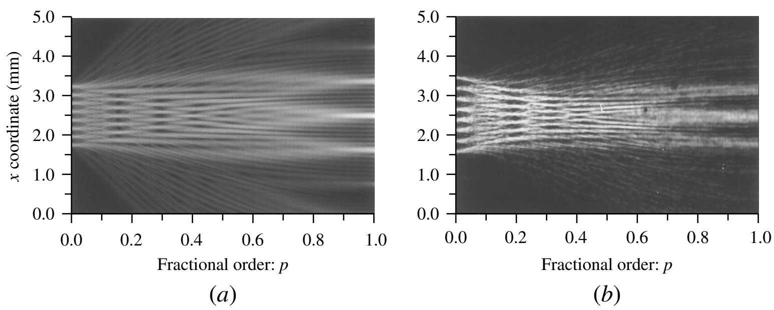

FIGURE 4.6 RWD of a Ronchi grating of 3 lines/mm: (a) exact numerical simulation; (b) experimental result.

simulations and the experimental results obtained using a Ronchi grating as input object.

Interestingly, in Fig. 4.6 the values of p that correspond to the self-images, both positive and negative, can be clearly identified. The optical setup designed for the experimental implementation of the RWD was successfully adapted to several applications, as we show later in this chapter.

In searching for an RWD with an exact scale factor for all the fractional orders, this approach also inspired another proposal[10] in which a bent structure for the detector was suggested. The result is an exact, but unfortunately impractical, setup to obtain the RWD. This drawback was partially overcome in other configurations derived by the same authors using the *abcd* matrix formalism. There, the free propagation distances are designed to be fixed or to vary linearly with the transverse coordinate,[11] so the input plane and/or the output plane should be tilted instead of bent, resulting in a more realistic configuration, provided that the tilt angles are measured very precisely.

4.3 Analysis of Optical Signals and Systems by Means of the RWT

4.3.1 Analysis of Diffraction Phenomena

4.3.1.1 Computation of Irradiance Distribution along Different Paths in Image Space

Determination of the irradiance at a given point in the image space of an imaging system is a classic problem in optics. The conventional techniques carry out a finite partition of the pupil of the system to sum all these contributions at the observation point.[12–16] This time-consuming procedure needs to be completely repeated for each observation point, or if the aberration state of the system changes. In this section we present a useful technique, based on the use of the RWT of a mapped version of the pupil of the system, for a much more efficient analysis of the irradiance in the image space of imaging systems. This technique has been successfully applied to the analysis of different optical systems with circular[17] as well as square,[18] elliptical,[19] triangular,[19] and even fractal pupils.[20] The method has also been applied to the study of multifacet imaging devices.[21]

Let us consider a general imaging system, characterized by an exit pupil function with generalized amplitude transmittance $P(\vec{x})$. The distance from this pupil to the Gaussian imaging plane is denoted by f. Note that the function $P(\vec{x})$ includes any arbitrary amplitude variation $p(\vec{x})$ and any phase aberration that the imaging system may suffer from.

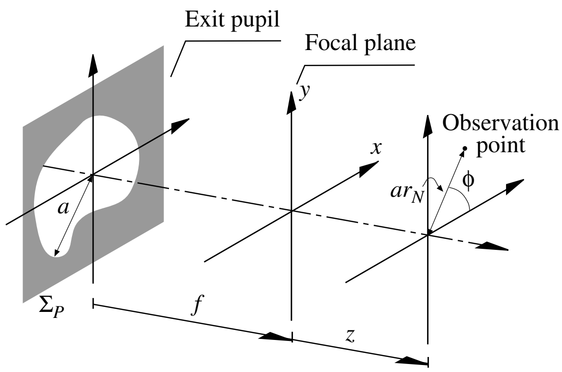

FIGURE 4.7 The imaging system under study.

We now describe the monochromatic scalar light field at any point of the image space of the system in the Fresnel approximation[21]. It is straightforward to show that, within this approach, the field irradiance is given by

$$I(\vec{x}, z) = \frac{1}{\lambda^2 (f+z)^2} \times \left| \iint_{\Sigma_P} P(\vec{x}') \exp\left[\frac{-i\pi z |\vec{x}'|^2}{\lambda f (f+z)}\right] \exp\left[\frac{-i2\pi}{\lambda(f+z)} \vec{x}\cdot\vec{x}'\right] d^2\vec{x}' \right|^2 \tag{4.48}$$

where λ is the field wavelength, $\vec{x}$ and z stand for the transverse and axial coordinates of the observation point, respectively, and Σ_P represents the pupil plane surface. The origin for the axial distances is fixed at the axial Gaussian point, as shown in Fig. 4.7.

It is convenient to express all transverse coordinates in normalized polar form, namely,

$$x = a r_N \cos\phi, \qquad y = a r_N \sin\phi \tag{4.49}$$

where x and y are Cartesian coordinates and a stands for the maximum radial extent of the pupil. By using these explicit coordinates in Eq. (4.48), we obtain

$$\begin{aligned} \bar{I}(r_N, \phi, z) &= \frac{1}{\lambda^2 (f+z)^2} \left| \int_0^{2\pi}\int_0^1 \bar{p}(r'_N, \phi') \exp\left[\frac{i2\pi W(r'_N, \phi')}{\lambda}\right] \exp\left[\frac{i2\pi W_{20}(z)\, r'^2_N}{\lambda}\right] \right. \\ &\quad \left. \times \exp\left[\frac{-i2\pi}{\lambda(f+z)} r'_N r_N \cos(\phi' - \phi)\right] r'_N\, dr'_N\, d\phi' \right|^2 \end{aligned} \tag{4.50}$$

where the bar denotes the polar coordinate expression for the corresponding function and where we have split out the generalized pupil $P(\vec{x})$ to explicitly show the dependence on the amplitude pupil variations $p(\vec{x})$ and the aberration function $W(r'_N, \phi')$ of the system. The classic defocus coefficient has also been introduced in this equation, namely,

$$W_{20}(z) = -\frac{za^2}{2f(f+z)} \tag{4.51}$$

In many practical situations the most important contribution to the aberration function is the primary *spherical aberration* (SA), whose dependence on the pupil coordinates is given by

$$W_{40}(r'_N, \phi') = W_{40} {r'_N}^4 \tag{4.52}$$

where W_{40} is the SA coefficient design constant. In the following reasoning, we will consider this term explicitly, splitting the generalized pupil of the system as follows:

$$\bar{p}(r'_N, \phi') \exp\left[\frac{i2\pi W(r'_N, \phi')}{\lambda}\right] = Q(r'_N, \phi') \exp\left[\frac{i2\pi W_{40}\, {r'_N}^4}{\lambda}\right] \tag{4.53}$$

Thus $Q(r'_N, \phi')$ includes the amplitude variations on the pupil plane and the aberration effects except for SA. Note that if no aberrations different from SA are present in the system, $Q(r'_N, \phi')$ reduces simply to the pupil mask $\bar{p}(r'_N, \phi')$.

By substituting Eq. (4.53) into Eq. (4.50), we finally obtain

$$\begin{aligned}\bar{I}(r_N, \phi, z) &= \frac{1}{\lambda^2 (f+z)^2} \left| \int_0^{2\pi} \int_0^1 Q(r'_N, \phi') \exp\left(\frac{i2\pi W_{40}\, {r'_N}^4}{\lambda}\right) \exp\left[\frac{i2\pi W_{20}(z)\, {r'_N}^2}{\lambda}\right] \right. \\ &\quad \left. \times \exp\left[\frac{-i2\pi}{\lambda(f+z)} r'_N r_N \cos(\phi' - \phi)\right] r'_N \, dr'_N \, d\phi' \right|^2\end{aligned} \tag{4.54}$$

Let us now consider explicitly the angular integration in this equation, namely,

$$Q(r'_N, r_N, \phi, z) = \int_0^{2\pi} Q(r'_N, \phi') \exp\left[\frac{-i2\pi}{\lambda(f+z)} r'_N r_N \cos(\phi' - \phi)\right] d\phi' \tag{4.55}$$

Thus we arrive at a compact form for the irradiance at a point in the image space

$$\bar{I}(r_N, \phi, z) = \frac{1}{\lambda^2 (f+z)^2} \times \left| \int_0^1 Q(r'_N, r_N, \phi, z) \exp\left(\frac{i2\pi W_{40} {r'_N}^4}{\lambda} \right) \exp\left[\frac{i2\pi W_{20}(z) {r'_N}^2}{\lambda} \right] r'_N \, dr'_N \right|^2 \tag{4.56}$$

By using the mapping transformation

$$ {r'_N}^2 = s + \frac{1}{2}, \qquad Q(r'_N, r_N, \phi, z) = q(s, r_N, \phi, z) \tag{4.57}$$

we finally obtain

$$\bar{I}(r_N, \phi, z) = \frac{1}{\lambda^2 (f+z)^2} \times \left| \int_{-0.5}^{0.5} q(s, r_N, \phi, z) \exp\left(\frac{i2\pi W_{40} s^2}{\lambda} \right) \exp\left\{ \frac{i2\pi [W_{40} + W_{20}(z)] s}{\lambda} \right\} ds \right|^2 \tag{4.58}$$

Note that in this expression all the dependence on the observation coordinates is concentrated in the mapped pupil $q(s, r_N, \phi, z)$ and the defocus coefficient $W_{20}(z)$. If we expand the modulus square in this equation, we find

$$\begin{aligned}\bar{I}(r_N, \phi, z) = {} & \frac{1}{\lambda^2 (f+z)^2} \\ & \times \int_{-0.5}^{0.5} \int_{-0.5}^{0.5} q(s, r_N, \phi, z) q^*(s', r_N, \phi, z) \exp\left[\frac{i2\pi W_{40} (s^2 - s'^2)}{\lambda} \right] \\ & \times \exp\left\{ \frac{i2\pi \, [W_{40} + W_{20}(z)\,] \,(s - s')}{\lambda} \right\} ds \, ds' \end{aligned} \tag{4.59}$$

which by using the change of variables

$$ t = \frac{s + s'}{2}, \qquad u = s - s' \tag{4.60}$$

can be rewritten as

$$\bar{I}(r_N, \phi, z) = \frac{1}{\lambda^2(f+z)^2}$$
$$\times \int_{-1}^{1}\int_{-0.5}^{0.5} q\left(t+\frac{u}{2}, r_N, \phi, z\right) q^*\left(t-\frac{u}{2}, r_N, \phi, z\right)$$
$$\times \exp\left\{\frac{i2\pi}{\lambda}\left[W_{40}+W_{20}(z)\ +2\xi W_{40}\right]u\right\} dt\, du \tag{4.61}$$

The above integration over the variable u can be clearly identified as the WDF of $q\ (s, r_N, \phi, z)$ with respect to the first variable, as stated in Eq. (4.1). Thus, it is straightforward to show that

$$\bar{I}(r_N, \theta, z) = \frac{1}{\lambda^2(f+z)^2}\int_{-0.5}^{0.5} W_q\left(t, -2\frac{W_{40}}{\lambda}t - \frac{W_{40}+W_{20}(z)}{\lambda}\right) dt \tag{4.62}$$

This expression relates the irradiance at any observation point to the line integral of the function $W_q\ (x, \xi)$ along a straight line in phase space described by the equation

$$\xi = -2\frac{W_{40}}{\lambda}x - \frac{W_{40}+W_{20}(z)}{\lambda} \tag{4.63}$$

as depicted in Fig. 4.8. One can identify this integration as a projection of the WDF at an angle θ given by [see Eq. (4.10)]

$$\tan\theta = -\frac{\lambda}{2W_{40}} \tag{4.64}$$

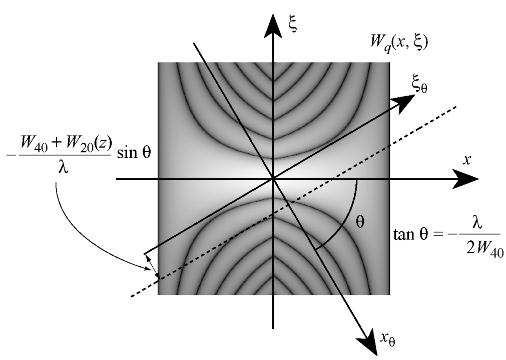

FIGURE 4.8 Integration line in phase space.

and at an oriented distance from the origin

$$x_\theta(z) = -\frac{W_{40} + W_{20}(z)}{\sqrt{4W_{40}^2 + \lambda^2}} \tag{4.65}$$

in such a way that it is possible to express

$$\bar{I}(r_N, \theta, z) = \frac{1}{\lambda^2(f+z)^2} RW_q\left(x_\theta(z), \theta\right) \tag{4.66}$$

The main conclusion of all this is that it is possible to obtain the irradiance at any point in image space through the values of the RWT of a given function $q(s, r_N, \phi, z)$ related to the pupil of the system. Note, however, that this function depends in general on the particular coordinates r_N, ϕ, and z of the observation point. Thus, a different function $RW_q(x_\theta, \theta)$ has to be considered for different points in image space. This major drawback can be overcome for special sets of points or trajectories in image space that share the same associated mapped pupil $q(s, r_N, \phi, z)$.

To describe such trajectories in image space, let us express these lines in parametric form $r_N(z)$, $\phi(z)$. By substituting Jacobi's identity

$$\exp(i\gamma\cos\chi) = \sum_{n=-\infty}^{+\infty} i^n J_n(\gamma)\exp\left(-in\chi\right) \quad \gamma, \chi \in \mathbb{R} \tag{4.67}$$

where $J_n(x)$ represents the Bessel function of the first kind and order n, into Eq. (4.55), it is straightforward to obtain

$$\begin{aligned} Q(r'_N, r_N(z), \phi(z), z) = &\sum_{n=-\infty}^{+\infty} i^n J_n\left(\frac{-2\pi}{\lambda(f+z)} r'_N r_N(z)\right) Q_n(r'_N) \\ &\times \exp\left[in\phi(z)\right] \end{aligned} \tag{4.68}$$

where $Q_n(r'_N)$ stands for the n-order circular harmonic of $Q_n(r'_N, \phi')$, that is,

$$Q_n(r'_N) = \int_0^{2\pi} Q(r'_N, \phi')\exp\left(-in\phi'\right) d\phi' \tag{4.69}$$

Note that the dependence on the position parameter z in Eq. (4.68) is established exclusively in the argument of the Bessel functions—through $r_N(z)$—and the phase exponentials—through $\phi(z)$. Thus, the only way to strictly cancel this dependence is to consider the trajectories

$$r_N(z) = K(f+z), \qquad \phi(z) = \phi_o \tag{4.70}$$

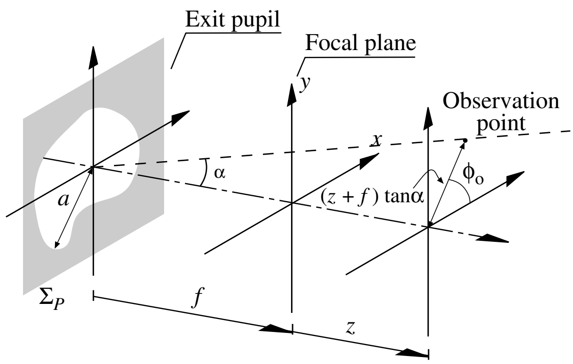

FIGURE 4.9 Trajectories in image space.

These curves correspond to straight lines passing through the axial point at the plane of the exit pupil. Together with the optical axis, each line defines a plane that forms an angle ϕ_o with the x axis, as depicted in Fig. 4.9. Note that the angle α of any of these lines with the optical axis is given by

$$\tan\alpha = Ka \tag{4.71}$$

For these subsets of observation points, the mapped pupil of the system can be expressed as

$$\begin{aligned} Q(r'_N, r_N(z), \phi(z), z) &= Q^{\alpha,\phi_o}(r'_N) \\ &= \sum_{n=-\infty}^{+\infty} i^n J_n\left(\frac{-2\pi a \tan\alpha}{\lambda} r'_N\right) Q_n(r'_N) \exp\left(in\phi_o\right) \end{aligned} \tag{4.72}$$

and analogously

$$r'^2_N = s + \frac{1}{2}, \quad q(s, r_N(z), \phi(z), z) = Q^{\alpha,\phi_o}(r'_N) = q^{\alpha,\phi_o}(s) \tag{4.73}$$

in such a way that now the corresponding RWT $RW_{q^{\alpha,\theta_o}}(x_\theta, \theta)$ is independent of the propagation parameter z. This is a very interesting issue since the calculation of the irradiance at any observation point lying on the considered line can be achieved from this single two-dimensional display by simply determining the particular coordinates $(x_\theta(z), \theta)$ through Eqs. (4.64) and (4.65). Furthermore, the proper choice of these straight paths allows one to obtain any desired partial feature of the whole three-dimensional image irradiance distribution. Note also that since W_{40} is just a parameter in these coordinates and does not affect the function $RW_{q^{\alpha,\theta_0}}(x_\theta, \theta)$, this single display can be used for the determination of the irradiance for different amounts of SA. Thus, compared to classic techniques, the reduction in computation time is evident. The axial irradiance distribution is often used as a figure of merit for the performance of optical systems with aberrations. This distribution can be obtained here as a particular case with $\alpha = 0$, namely,

$$I(0, 0, z) = \frac{1}{\lambda^2(f + z)^2} RW_{q^{0,0}}(x_\theta(z), \theta) \tag{4.74}$$

where

$$q^{0,0}(s) = Q^{0,0}(r'_N) = Q_0(r'_N) \tag{4.75}$$

This result is especially interesting since this mapped pupil, and thus the associated RWT, is also independent of the wavelength λ. This fact represents an additional advantage when a polychromatic assessment of the imaging system is needed, as will be shown in forthcoming sections. Some quantitative estimation of these improvements is presented in Ref. 19.

To prove the performance of this computation method, next we present the result of the computation of the irradiance distribution along different lines in image space of two imaging systems, labeled system I and system II. For the sake of simplicity, we consider only purely absorbing pupils and no aberrations apart from SA in both cases. Thus, $Q(r'_N, \phi')$ reduces to the normalized pupil function $\bar{p}(r'_N, \phi')$. A gray-scale representation for the pure absorbing masks considered for each system is shown in Fig. 4.10.

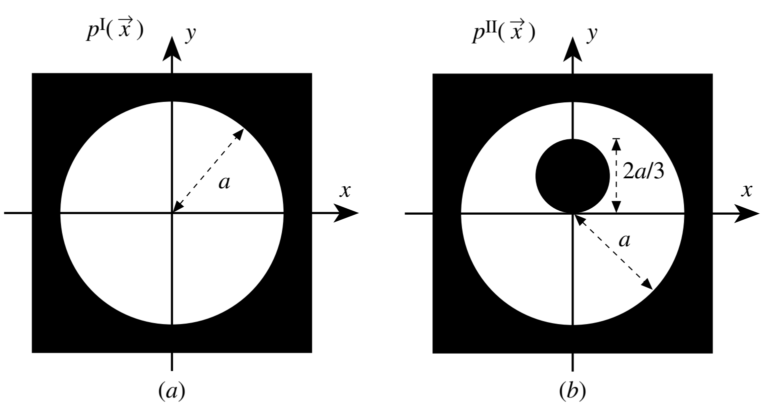

FIGURE 4.10 Gray-scale picture of the pupil functions for (*a*) system I and (*b*) system II.

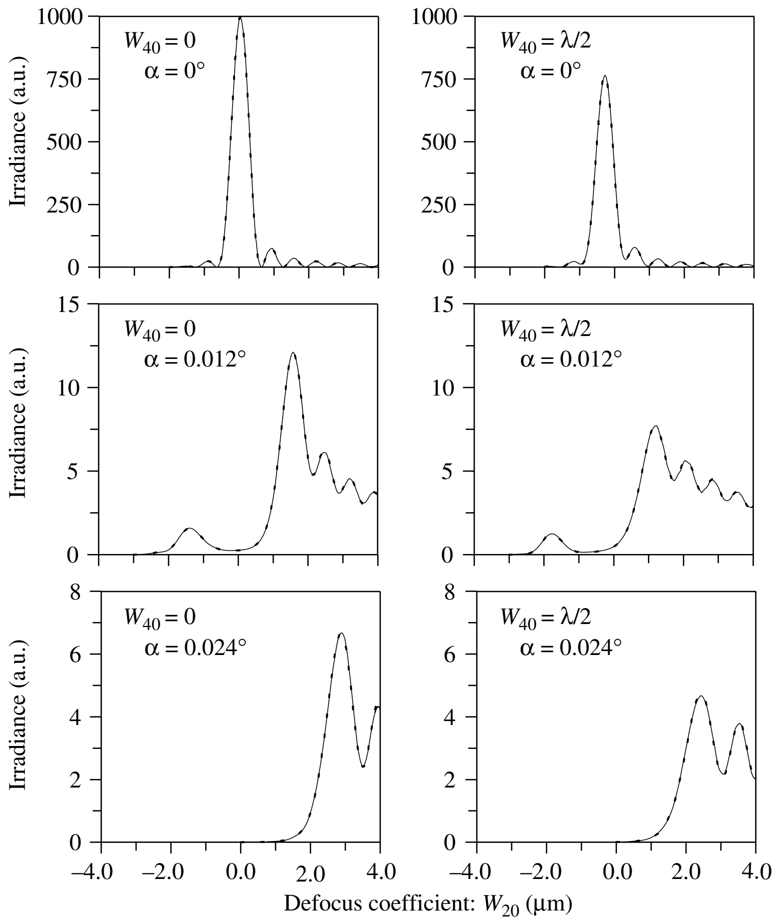

FIGURE 4.11 Irradiance values provided by system I, along different lines containing the axial point of the pupil and for two different amounts of SA. Continuous lines represent the result by the proposed RWT method while dotted lines stand for the computation by the classic method.

We compute the irradiance values for 256 points along three different lines passing through the axial point of the pupil, all characterized by an azimuthal angle $\phi_o = \pi/2$. These trajectories are chosen with tilt angles $\alpha = 0.024°$, $0.012°$ and $0°$ (optical axis). We set $a = 10$ mm, $z = 15.8$ mm, and $\lambda = 638.2$ nm. The function $RW_{q^{\alpha,\theta_o}}(x_\theta, \theta)$ was computed for 4096×4096 points, and for comparison purposes, the same irradiance values were computed by using the classic method[12,13] by partitioning the exit pupil of the imaging system into 1024×1024 radial-azimuthal elements. Figure 4.11 shows a joint representation of

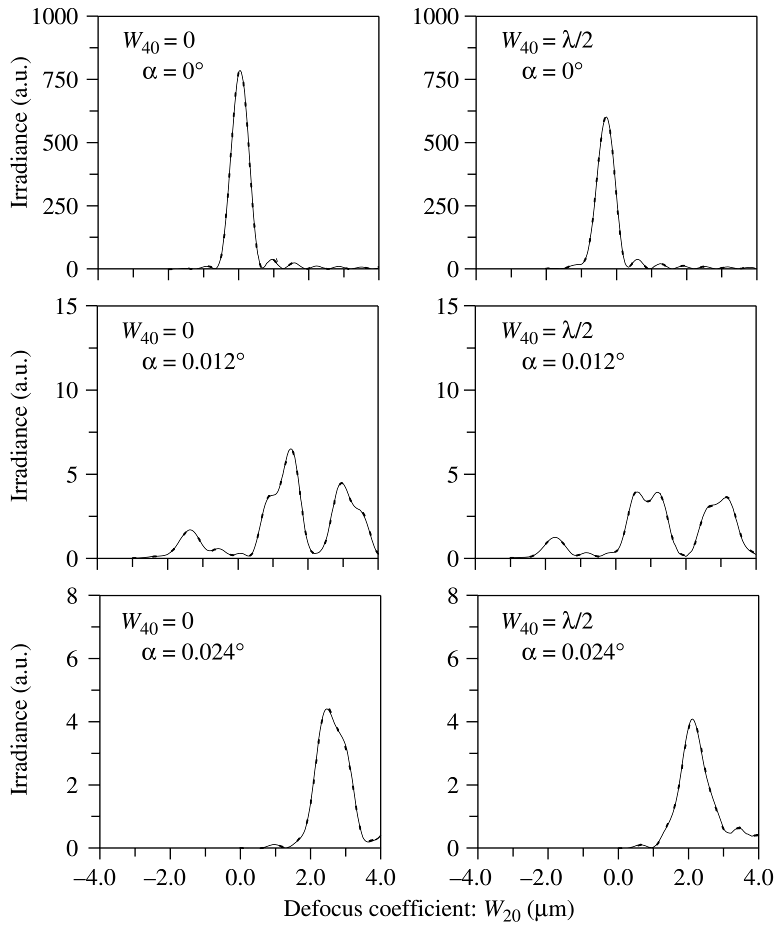

FIGURE 4.12 Irradiance values provided by system II, as in Fig. 4.11.

the numerical calculation for system I, when two different values of the SA are considered. The same results applied now to system II are presented in Fig. 4.12.

The analysis of these pictures shows that the results obtained with the RWT method match closely those obtained with the classic technique. In fact, both results differ by less than 0.03 percent. However, the RWT is much more efficient in this computation process. This is so because the basic RWT does not require recalculation for any point in each of the curves. This is also true for any amount of SA. Obviously, the greater the number of observation points, or SA values, that have to be considered, the greater the resultant savings in computation time.

As a final remark on this subject, we want to point out that this approach can also be applied to other trajectories of interest in image space. For instance, short paths parallel to the optical axis in the neighborhood of the focal plane[17] or straight lines crossing the focal point can be considered.[22]

4.3.1.2 Parallel Optical Display of Diffraction Patterns

In Sec. 4.2.2 we mentioned that the mathematical relationship between Fresnel diffraction and the FrFT is given by Eq. (4.41). This means that the RWD is itself a continuous display of the evolution of diffraction patterns of one-dimensional objects, and this property is extremely useful from a pedagogical point of view. In fact, calculations of Fresnel and Fraunhofer diffraction patterns of uniformly illuminated one-dimensional apertures are standard topics in undergraduate optics courses. These theoretical predictions are calculated analytically for some typical apertures, or, more frequently, they are computed numerically. The evolution of these diffraction patterns under propagation is often represented in a two-dimensional display of gray levels in which one axis represents the transverse coordinate—pattern profile—and the other axis is related to the axial coordinate—evolution parameter.[23] This kind of representation illustrates, e.g., how the geometrical shadow of the object transforms into the Fraunhofer diffraction pattern as it propagates, and that the Fraunhofer diffraction simply is a limiting case of Fresnel diffraction.[24] In addition to the qualitative physical insight that the RWD provides about diffraction, it can provide a quantitative measurement of a variety of terms. These include the precise location y_s and the relative magnification M_s of each diffraction pattern. These two terms are quantitatively defined in terms of the maximum φ_h and minimum φ_0 powers of the varifocal lens L of the system represented in Fig. 4.5, i.e.,

$$y_s = \frac{hs}{s + l^2(\varphi_h - \varphi_0)}, \qquad M_s = 1 + \frac{s}{l^2(\varphi_h - \varphi_0)} \tag{4.76}$$

where s is the axial coordinate at which the corresponding diffraction pattern is localized under parallel illumination and h is the extent of the so-called progression zone of the varifocal lens. Figure 4.13 illustrates the experimental results registered by a CCD camera using a double slit as an input object. It can be seen that the RWD is a nice representation of the evolution by propagation of the interference phenomena. In fact, the Fraunhofer region of the diffracted field clearly shows the characteristic Young fringes modulated by a sinc function. To compare the theoretical and experimental results, a cross section of

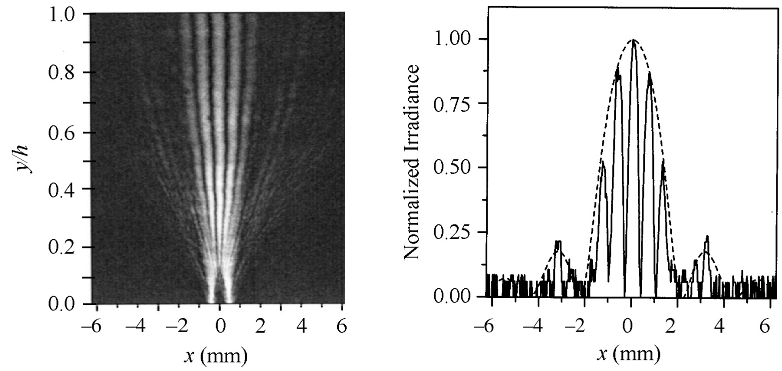

FIGURE 4.13 RDW showing the evolution of the field diffracted by a double slit. (*a*) Experimental result. (*b*) Cross section of the RWD showing the intensity profile near the Fraunhofer region. For comparison purposes, the theoretical sinc envelope of the Young fringes is also shown by the dotted line.

the experimental RWD for values of y/h close to 1 is also represented in Fig. 4.13.

Another classic example is diffraction by periodic objects. Here, self-imaging phenomena, such as the Talbot effect, are interesting and stimulating and usually attract the students' attention. As illustrated earlier in Fig. 4.6, which shows the diffraction patterns of a Ronchi grating, several self-imaging planes can be identified. It can be clearly seen that, due to the finite extent of the grating at the input, the number of Talbot images is limited by the so-called walk-off effect. Self imaging phenomena are discussed in more detail in Chapter 9 by Markus Testorf.

In addition to its use as an educational tool for displaying diffraction patterns, the RWD has been used to investigate diffraction by a variety of different interesting structures including fractal diffraction screens. In fact, the properties of diffraction patterns produced by fractal objects and their potential applications have attracted the attention of several researchers during recent years because many natural phenomena and physical structures, such as phase transition, turbulence, or optical textures, can be analyzed and described by assuming fractal symmetry. Most research has been devoted to the study of diffraction patterns obtained from fractal objects in the Fraunhofer region,[25] yet it is in the Fresnel region where interesting features appear. For instance, Fresnel diffraction of a Cantor set[26] shows an irradiance distribution along the optical axis having a periodicity that depends on the level of the set. Furthermore, the intensity distributions at transverse planes

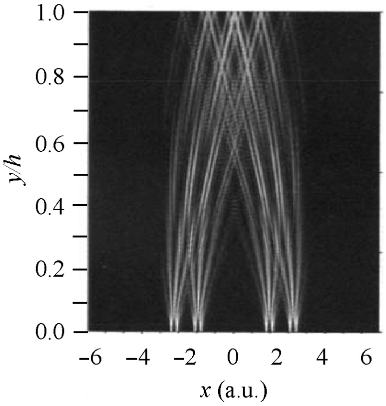

FIGURE 4.14 RWD as a display of all diffraction patterns generated by a Cantor grating of level 3.

show a partial self-similar behavior that is increased when moving toward the Fraunhofer region. For this reason, it is useful to represent the evolution of the complex amplitude of one-dimensional fractals propagating through free space represented on a two-dimensional display, especially if such a display can be obtained experimentally. In this case one axis represents the transversal coordinate, and the other is a function of the axial coordinate. In fact, according to the analysis carried out in Ref. 27, the evolution of the diffraction patterns allows one to determine the main characteristic parameters of the fractal. Therefore, one of the most important applications of the RWD has been in this field.[28] The RWD obtained for a triadic Cantor grating developed up to level 3 is shown in Fig. 4.14. Moreover, this result can be favorably compared with the results obtained with other displays.[27] The magnification provided by the lens L in the experimental setup (see Fig. 4.4) enables the RWD representation to provide an optimum sampling of the diffracted field. Near the object, where the diffraction patterns change rapidly, the mapping of the propagation distance provides a fine sampling, whereas the sampling is coarse in the far field where the variation of the diffraction patterns with the axial distance is slow. We note that sampling is the subject of Chapter 10.

4.3.2 Inverting RWT: Phase-Space Tomographic Reconstruction of Optical Fields

The WDF is an elegant and graphical way to describe the propagation of optical fields through linear systems. Since the WDF of a complex field distribution contains all the necessary information to retrieve the field itself,[29,30] many of the methods to obtain the WDF (and the AF)

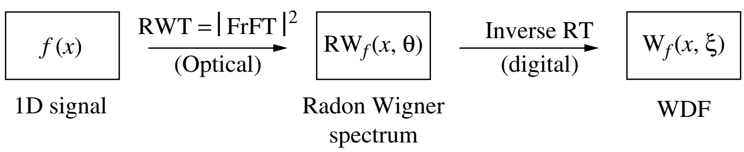

FIGURE 4.15 Diagram of the proposed hybrid optodigital method.

could be adapted to solve the phase retrieval problem. Optical or optoelectronic devices are the most commonly employed systems to obtain a representation of phase-space functions of one-dimensional or two-dimensional complex signals.[31,32] However, because most detectors used to this end are only sensitive to the incident intensity, interferometric or iterative methods are necessary in general to avoid loss of information. This is true even for the optically obtained WDF, which is real but has, in general, negative values and therefore is obtained from an intensity detector with an uncertainty in its sign. On the other hand, obtaining the WDF of wave fields is also possible indirectly through other representations such as the Radon transform.[33] In this particular case, a tomographic reconstruction is needed to synthesize the WDF. With this information it is possible to recover the amplitude and the phase of the original field distribution solely by means of intensity measurements. With most experimental setups for phase retrieval,[29,30] these measurements have to be taken sequentially in time while varying the distances between some components in each measurement. In this way the potential advantage of optics, i.e., parallel processing of signal information, is wasted. Consequently, another interesting application of the setup discussed in Sec. 4.2.2 to obtain the RWD is the experimental recovery of the WDF by means of an inverse Radon transformation.

The technique to obtain the WDF from projections is divided into two basic stages, sketched in Fig. 4.15. In the first stage, the experimental Radon-Wigner spectrum of the input function is obtained from a two-dimensional single-shot intensity measurement by the use of the experimental setup in Fig. 4.4. This optical method benefits from having no moving parts.

The second part of the proposed method is the digital computation of the inverse Radon transforms of the experimental Radon-Wigner spectrum. The most common algorithms used in tomographic reconstruction are based on the technique known as filtered backprojection. This algorithm is based on the *central slice theorem* discussed in Sec. 4.2.1. Thus, from Eqs. (4.21) and (4.22) we have

$$\mathcal{F}\{RW_f(x_\theta, \theta), \xi_\theta\} = \mathcal{F}_{2\mathrm{D}}\{W_f(x, \xi), (x_\theta \cos\theta, \xi_\theta \sin\theta)\} \qquad (4.77)$$

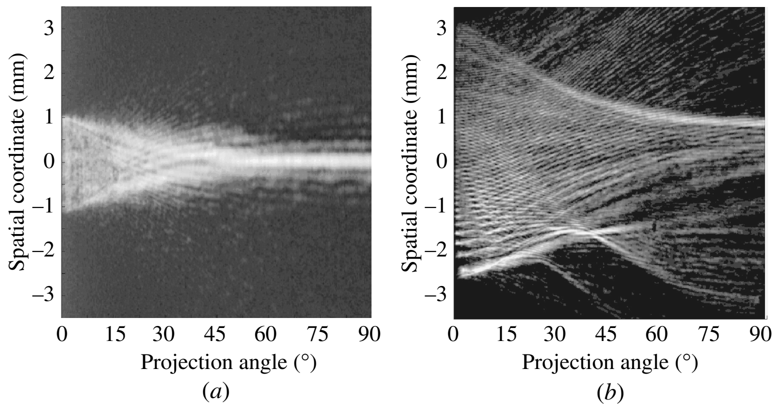

FIGURE 4.16 Experimental Radon-Wigner spectrum of (*a*) a single slit of 2.2 mm and (*b*) a binary grating with a linearly increasing spatial frequency.

where the one-dimensional FT is performed on the first argument of $RW_f(x_\theta, \theta)$. The inversion of this last transformation allows the recovery of $W_f(x, \xi)$ from its projections. Explicitly[34]

$$W_f(x, \xi) = \int_0^\pi C_f(x \cos\theta + \xi \sin\theta, \theta)\, d\theta \tag{4.78}$$

with

$$C_f(u, \theta) = \int_{-\infty}^{+\infty} \mathcal{F}\{RW_f(x_\theta, \theta), \xi_\theta\}\, |\xi_\theta| \exp(i2\pi\xi_\theta u)\, d\xi_\theta \tag{4.79}$$

Equation (4.79) can be clearly identified as a filtered version of the original RWT. In this way, from Eq. (4.78), $W_f(x, \xi)$ is reconstructed for each phase-space point as the superposition of all the projections passing through this point.

The experimental RWD of different one-dimensional functions has been used to reconstruct the WDF from projections. In Fig. 4.16 we show the RWD obtained with the optical device described in Sec. 4.2.2 for two different functions, namely, a rectangular aperture (single slit) and a grating with a linearly increasing spatial frequency (*chirp* signal).

To undertake the reconstruction of the WDF through the filtered backprojection algorithm, it is necessary to consider the complete angular region of the RWD, that is, $\theta \in [0, \pi)$. Although we only obtain optically the RWT for $\theta \in [0, \pi/2]$, the symmetry property in Eq. (4.17) has been used to complete the spectrum. From the experimental RWD

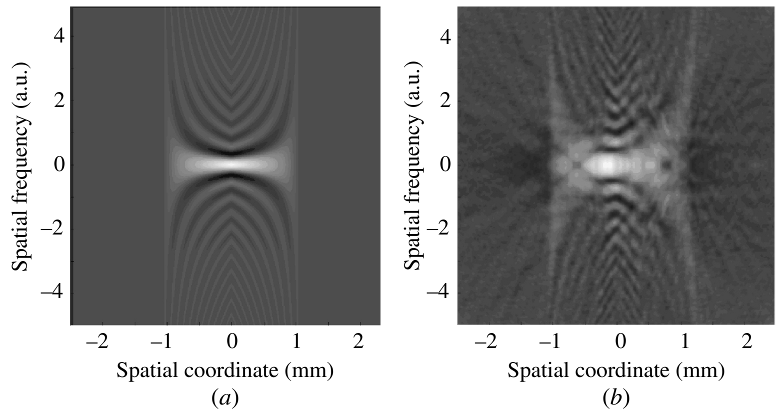

FIGURE 4.17 (*a*) Theoretical WDF of a single slit. (*b*) Experimental result for the tomographic reconstruction of the WDF of the same slit.

in Fig. 4.16, the corresponding WDFs have been obtained using the filtered backprojection algorithm. For comparison purposes, Figs. 4.17 and 4.18 show both the theoretical and the experimentally reconstructed WDF of the single slit and the chirp grating, respectively. Note that in Figs. 4.17*b* and 4.18*b* some artifacts appear. The lines radiating from the center and outward are typical artifacts (*ringing effect*) associated with the filtered backprojection method.[35] In spite of this

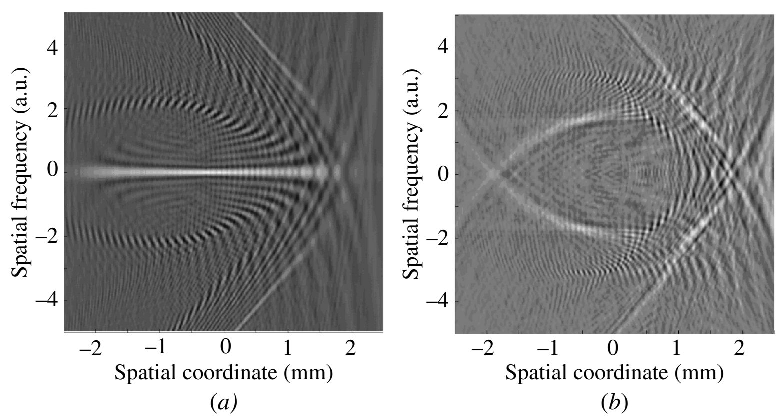

FIGURE 4.18 (*a*) Theoretical WDF of a binary grating with a linearly increasing spatial frequency. (*b*) Experimental tomographic reconstruction of the WDF of the same grating.

effect, a very good qualitative agreement can be observed between the results obtained with the theoretical and experimental data. The asymmetry in Fig. 4.17 is a consequence of the noise in Fig. 4.16*a*, reflecting also the asymmetry on the spatial coordinate in this figure. In Fig. 4.18 the typical arrow-shaped WDF of a chirp function can be observed in both cases. The slope in the arrowhead that characterizes the chirp rate of the signal is the same for the theoretical and the experimental results.

Several extensions of the proposed method are straightforward. On one hand, a similar implementation proposed here for the WDF can be easily derived for the AF, by virtue of Eq. (4.22). Note also that it is easy to extend this method to obtain two-dimensional samples of the four-dimensional WDF of a complex two-dimensional signal by use of a line scanning system. Moreover, since complex optical wave fields can be reconstructed from the WDF provided the inversion formulas, this approach can be used as a phase retrieval method that is an alternative to the conventional interferometric or iterative-algorithm-based techniques. In fact, as demonstrated,[36] phase retrieval is possible with intensity measurements at two close FrFT domains. This approach, however, requires some a priori knowledge of the signal bandwidth. In our method, a continuous set of FrFTs is available simultaneously, and this redundancy should avoid any previous hypothesis about the input signal.

4.3.3 Merit Functions of Imaging Systems in Terms of the RWT

4.3.3.1 Axial Point-Spread Function (PSF) and Optical Transfer Function (OTF)

There are several criteria for analyzing the performance of an optical imaging system for aberrations and/or focus errors in which the on-axis image intensity, or axial point-spread function (PSF), is the relevant quantity. Among them we mention:[37] Rayleigh's criterion, Marechal's treatment of tolerance, and the Strehl ratio (SR). As Hopkins suggested,[38] the analysis of Marechal can be reformulated to give a tolerance criterion based on the behavior of the optical transfer function (OTF) (spatial frequency information) instead of the PSF (space information). Phase-space functions were also employed to evaluate some merit functions and quality parameters.[39–41] This point of view equally emphasizes both the spatial and the spectral information contents of the diffracted wave fields that propagate in the optical imaging systems. Particularly, since the information content stored in the FrFT of an input signal changes from purely spatial to purely spectral as p varies from $p = 0$ to $p = 1$, that is, in the domain of the RWT, it is expected that the imaging properties of a given optical system, in both the space and spatial frequency domains, could also be evaluated from the RWD.

To derive the formal relationship between the PSF (and the OTF) and the RWT, let us consider the monochromatic wave field, with wavelength λ, generated by an optical imaging system characterized by a one-dimensional pupil function $t(x)$, when a unit amplitude point source is located at the object plane.In the neighborhood of the image plane, located at $z = 0$, the field amplitude distribution can be written, according to the Fresnel scalar approximation, as

$$U(x, z) = \int_{-\infty}^{+\infty} t(x') \exp\left(\frac{-i\pi}{\lambda f} x'^2\right) \exp\left[\frac{i\pi}{\lambda(f+z)}(x'-x)^2\right] dx' \tag{4.80}$$

where f is the distance from the pupil to the image plane. The transformation of $t(x)$ to obtain the field $U(x, z)$ is given by a two-step sequence of elementary *abcd* transforms, namely, a spherical wavefront illumination (with focus at $\eta = f$) and a free-space propagation (for a distance $f + z$). Considering the results presented in Sec. 4.2.1, the *abcd* matrix associated with this transform can be found to be

$$M = \begin{pmatrix} 1 & 0 \\ \frac{1}{\lambda f} & 1 \end{pmatrix} \begin{pmatrix} 1 & -\lambda(f+z) \\ 0 & 1 \end{pmatrix} = \begin{pmatrix} 1 & -\lambda(f+z) \\ \frac{1}{\lambda f} & -\frac{z}{f} \end{pmatrix} \tag{4.81}$$

and, therefore, the equivalent relationships to that given by Eq. (4.80) in terms of the corresponding RWTs can be expressed as [see Eq. (4.25)]

$$\begin{gathered} RW_{U(x,z)}(x_\theta, \theta) \propto RW_t(x_{\theta'}, \theta') \\ \tan\theta' = \frac{\lambda f \tan\theta - \lambda^2 f(f+z)}{\tan\theta - \lambda z}, \qquad x_{\theta'} = \frac{x_\theta}{\sin\theta + \lambda(f+z)\cos\theta} \sin\theta' \end{gathered} \tag{4.82}$$

In particular, the value $\theta = 0$ provides the irradiance distribution at the considered observation point, as stated in Sec. 4.2.1. This function is the PSF of the imaging system, as a function of the distance z to the image plane. Thus,

$$\begin{gathered} RW_{U(x,z)}(x_0, 0) = |U(x_0, z)|^2 = I(x_0, z) \propto RW_t(x_{\theta'_0}, \theta'_0) \\ \tan\theta'_0 = \frac{\lambda f(f+z)}{z}, \qquad x_{\theta'_0} = \frac{x_0}{\lambda(f+z)} \sin\theta'_0 \end{gathered} \tag{4.83}$$

For the optical axis ($x_0 = 0$) the PSF can be expressed as

$$RW_{U(x,z)}(0, 0) = |U(0, z)|^2 = I(0, z) \propto RW_t\left(0, \arctan\left[\frac{\lambda f(f+z)}{z}\right]\right) \tag{4.84}$$

A normalized version of this axial irradiance is often used as a figure of merit of the performance of the imaging system, namely, the SR versus defocus, defined as

$$S(W_{20}) = \frac{I(0, z)}{I(0, 0)} \propto RW_t \left(0, \arctan\left(-\frac{\lambda h^2}{2W_{20}}\right)\right) \tag{4.85}$$

where h is the maximum lateral extent of the one-dimensional pupil and W_{20} stands for the one-dimensional version of the defocus coefficient defined in Eq. (4.51). Thus, the function $S(W_{20})$ can be analyzed in a polar fashion in the two-dimensional domain of the WDF associated with the pupil function $t(x)$ or, equivalently, in terms of its associated RWT.

To illustrate this approach, the defocus tolerance of different kinds of one-dimensional pupils was investigated, namely, a clear aperture (slit) and a pupil with a central obscuration (double slit). The general form of these pupils can be written as $t(x) = \text{rect}(x/h) - \text{rect}(x/b)$, with $b = 0$ for the uniform aperture. Figure 4.19 shows the RWD

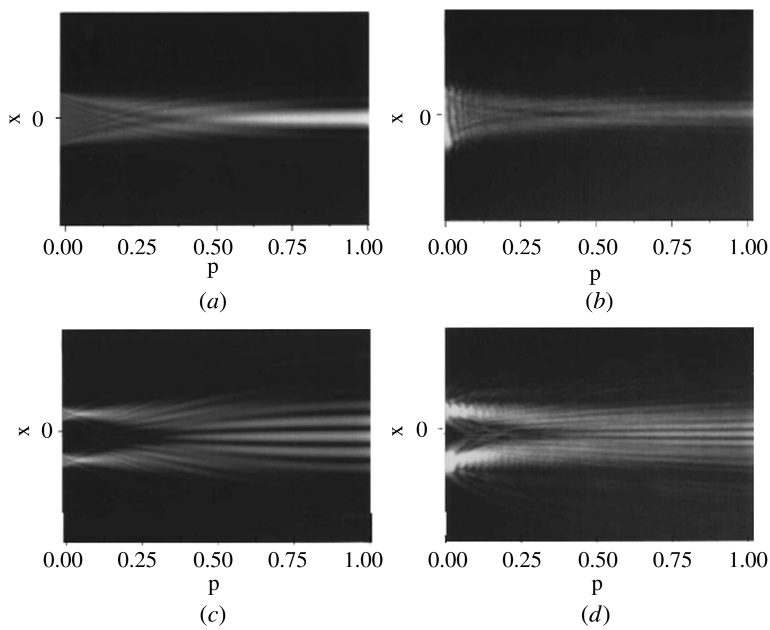

FIGURE 4.19 RWTs: (*a*) Computer simulation for an aperture with $a = 2.5$ mm and $b = 0$ mm. (*b*) Experimental result for (*a*). (*c*) Computer simulation for an aperture with $a = 2.5$ mm and $b = 1.3$ mm. (*d*) Experimental result for (*c*). The horizontal axis corresponds to the parameterization of the projection angle $\theta = p\pi/2$.

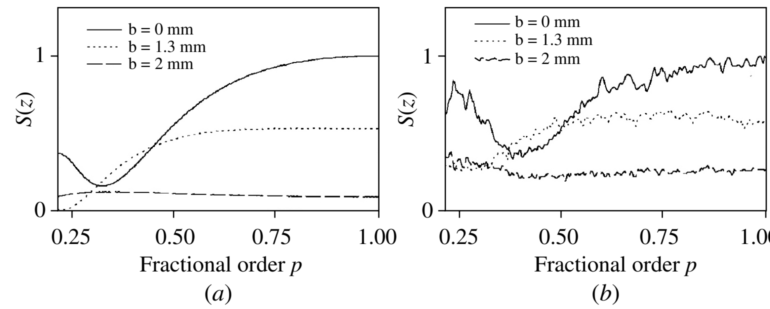

FIGURE 4.20 SR versus defocus for circular pupils with pupil function $t(x) = \mathrm{rect}(x/h) - \mathrm{rect}(x/b)$: (*a*) Computer simulation; (*b*) experimental results. Again, the projection angle $\theta = p\pi/2$.

numerically (parts *a* and *c*) and experimentally (parts *b* and *d*) obtained, for two different values of the obscuration *b*.

According to our previous discussion, the slices of the RWD for $x = 0$ give rise to the SR for variable W_{20}. These profiles are plotted in Fig. 4.20 for three different pupils. From these results, it can be observed that, as expected, annular apertures have higher tolerance to defocus.

The knowledge of the SR is useful to characterize some basic features of any optical system, such as the depth of focus. However, the main shortcoming of the SR as a method of image assessment is that although it is relatively easy to calculate for an optical design prescription, it is normally difficult to measure for a real optical system. Moreover, the quality of the image itself is better described through the associated OTF. Fortunately, this information can also be obtained from the RWD via its relationship with the AF established in Sec. 4.2.1, since the AF contains all the OTFs $H(\xi; W_{20})$ associated with the optical system with varying focus errors according to the formula[42]

$$H_\lambda(\xi; W_{20}) = A_t\left(-\lambda(f+z)\xi, \frac{2W_{20}(f+z)}{h^2}\xi\right) \tag{4.86}$$

In this way, the AF of the pupil function $t(x)$ can be interpreted as a continuous polar display of the defocused OTFs of the system. Conversely,

$$A_t\left(x', \xi'\right) = H_\lambda\left(-\frac{x'}{\lambda(f+z)}; W_{20} = -\frac{\lambda h^2 \xi'}{2x'}\right) \tag{4.87}$$

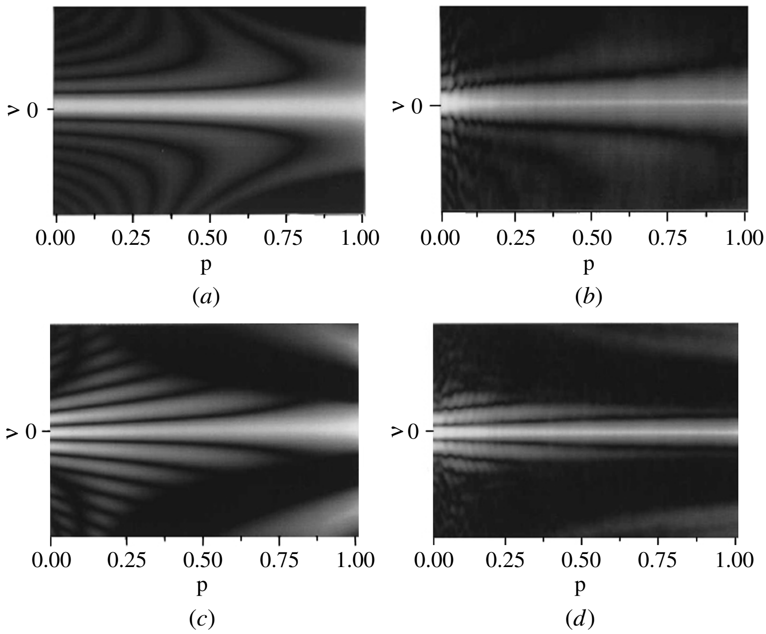

FIGURE 4.21 Computed one-dimensional FT of the RWDs shown in Fig. 4.19.

Thus, by using Eq. (4.22) it is easy to find that

$$\begin{aligned}\mathcal{F}\{RW_t(x_\theta, \theta), \xi_\theta\} &= A_t\,(\xi_\theta \cos\theta, -\xi_\theta \sin\theta) \\ &= H_\lambda\left(-\frac{\xi_\theta \cos\theta}{\lambda(f+z)}; W_{20} = \frac{\lambda h^2}{2}\tan\theta\right) \qquad (4.88)\end{aligned}$$

Therefore, the one-dimensional FT of the profile of the RWD for a given value of the fractional order $\theta = p\pi/2$ corresponds to a defocused (scaled) OTF. This representation is quite convenient to visualize Hopkins' criterion.[39]

Figure 4.21 shows the one-dimensional Fourier transforms, taken with respect to the x axis, of the RWT illustrated in Fig. 4.19. From the previous analysis, the defocused OTFs are displayed along the vertical or spatial-frequency axis. These results for the clear aperture are shown in Fig. 4.22.

The RWD can also be used for calculating the OTF of an optical system designed to work under polychromatic illumination. In this case, as we will discuss next, a single RWD can be used to obtain the set of monochromatic OTFs necessary for its calculation.

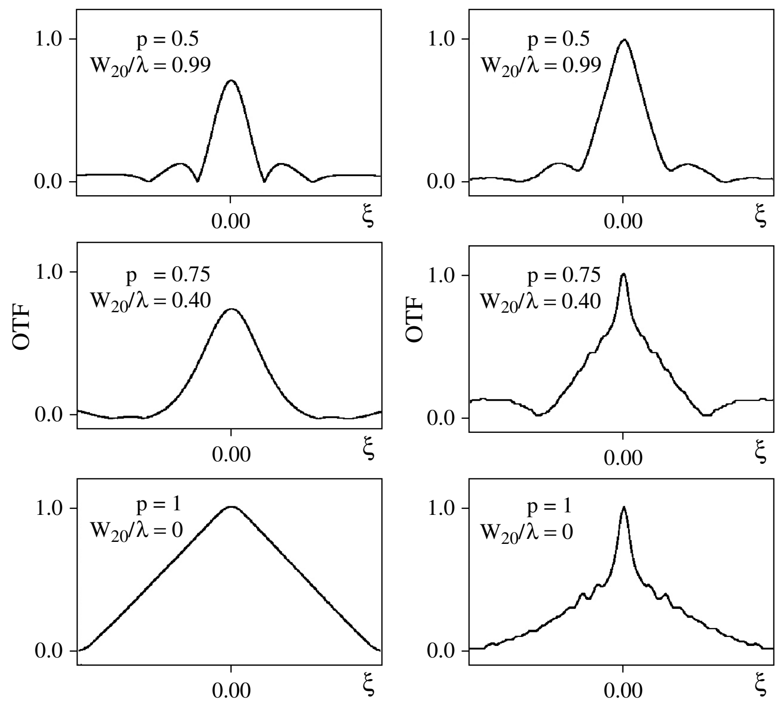

FIGURE 4.22 OTFs obtained from different slices of the intensity distributions shown in Fig. 4.21 for the case of a uniform aperture, for different amount of defocus.

4.3.3.2 Polychromatic OTF

As stated above, the RWT associated with the one-dimensional pupil of an imaging system can be used to obtain the OTF of the device, as a function of the defocus coefficient, through Eq. (4.88). It is worth noting that in this equation the wavelength λ of the incoming light acts as a parameter in the determination of the particular coordinates of the FT of the RWT, but it does not affect the RWT itself. Thus, changing the value of λ simply resets the position inside the same two-dimensional display for the computation of the OTF. The calculation procedure used in the previous section can be used, therefore, to compute the transfer function for any wavelength by means of the same RWD. This approach is based on previous work, where it was shown that the AF of the generalized pupil function of the system is a display of all the monochromatic OTFs with longitudinal chromatic aberration.[43]

An especially interesting application of this technique is the evaluation of the spatial-frequency behavior of optical systems working under polychromatic evaluation. In fact, the proper generalization of the OTF-based description to this broadband illumination case allows one to define quality criteria for imaging systems working with color signals.[44,45] This extension presents, however, some difficulties. The direct comparison of the incoming and the outgoing polychromatic irradiance distributions does not allow, in general, a similar relationship to the monochromatic case to be established. It can be shown, in fact, that only when the input signal is spectrally uniform can the frequency contents of both signals be related through a single polychromatic OTF function, providing the imaging system does not suffer from any chromatic aberrations regarding magnification.[46,47] Under these restrictions, a single polychromatic OTF can be used for relating input and output polychromatic irradiances in spatial-frequency space. This function is defined as

$$\mathcal{H}(\xi; W_{20}) = \frac{\int\limits_{\Lambda} H_{\lambda}(\xi; W'_{20}(\lambda))\, S(\lambda)\, V(\lambda)\, d\lambda}{\int\limits_{\Lambda} S(\lambda)\, V(\lambda)\, d\lambda} \tag{4.89}$$

where Λ and $S(\lambda)$ are the spectral range and the spectral power of the illumination, respectively. The function $V(\lambda)$ represents the spectral sensitivity of the irradiance detector used to record the image. Note also that a new wavelength-dependent defocus coefficient has been defined, to account for the longitudinal chromatic aberration $\delta W_{20}(\lambda)$ that the system may suffer from, namely,

$$W'_{20}(\lambda) = W_{20} + \delta W_{20}(\lambda) \tag{4.90}$$

where W_{20} is the defocus coefficient defined in the previous section.

This OTF cannot account, however, for the chromatic information of the image, since only a single detector is assumed.[48] Indeed, by following the trichromacy of the human eye, three different chromatic channels are usually employed to properly describe color features in irradiance distributions, and, consequently, three different polychromatic OTFs are used, namely,[44,45]

$$\begin{aligned}
\mathcal{H}(\xi; W_{20}) &= \frac{\int\limits_{\Lambda} H_{\lambda}(\xi; W'_{20}(\lambda))\, S(\lambda) x_{\lambda}\, d\lambda}{\int\limits_{\Lambda} S(\lambda) x_{\lambda}\, d\lambda} \\
\mathcal{H}(\xi; W_{20}) &= \frac{\int\limits_{\Lambda} H_{\lambda}(\xi; W'_{20}(\lambda))\, S(\lambda) y_{\lambda}\, d\lambda}{\int\limits_{\Lambda} S(\lambda) y_{\lambda}\, d\lambda} \\
\mathcal{H}(\xi; W_{20}) &= \frac{\int\limits_{\Lambda} H_{\lambda}(\xi; W'_{20}(\lambda))\, S(\lambda) z_{\lambda}\, d\lambda}{\int\limits_{\Lambda} S(\lambda) z_{\lambda}\, d\lambda}
\end{aligned} \tag{4.91}$$

where x_λ, y_λ, and z_λ are three spectral sensitivity functions associated with the measured chromaticity. These functions depend, obviously, on the specific color detector actually used. In the case of a conventional digital color camera, these channels can be associated with the R, G, and B bands of the three pixel families in the detector array. On the other hand, when a visual inspection of the final image is considered, these sensitivity functions are the well-known spectral tristimulus values of the human eye.[49]

Equations (4.91) establish the formulas to describe completely the response of a system from a spatial-frequency point of view. To numerically compute the functions described there, the evaluation of the monochromatic OTFs for a sufficient number of wavelengths inside the illumination spectrum has to be performed. Since any of these monochromatic transfer functions can be obtained from a same single RWD, as stated in the previous section, these computations can be done in a much more efficient way by use of this two-dimensional display. Furthermore, the same imaging system (i.e., the same pupil function) but suffering from different longitudinal chromatic aberration can be assessed as well, with no additional computation of the RWD. This is a critical issue in the saving of computation time which provides this technique with a great advantage compared to other classic techniques, as cited above.

To illustrate this technique, we present the result of the computation of the polychromatic OTFs associated with a conventional one-dimensional clear-pupil optical system (slit of width h) but suffering from two different chromatic aberration states (systems I and II from now on), as shown in Fig. 4.23. We assume that no other aberrations

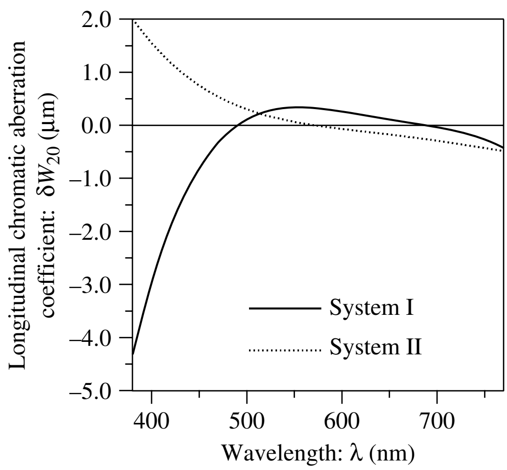

FIGURE 4.23 Longitudinal chromatic aberration coefficient associated with the two different correction states of the system under study.

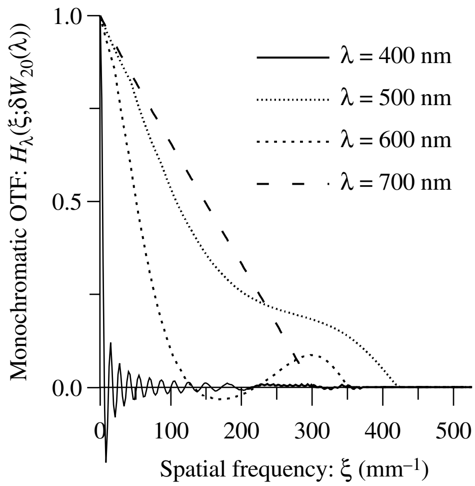

FIGURE 4.24 Monochromatic OTFs for system I in Fig. 4.23, corresponding to the imaging plane ($W_{20} = 0$).

are present. This assumption does not imply any restriction of the method, and the same applies to the one-dimensional character of the imaging system, as can be easily shown. Regarding the geometric parameters of the system, we fixed $h/f = 0.2$.

The evaluation of the corresponding monochromatic OTFs for both aberration states is achieved through the same computation method as in the previous section, namely, through the sequential one-dimensional FT of the two-dimensional display of the RWT $RW_t(x_\theta, \theta)$. Some of these results are shown in Fig. 4.24.

The computation of the polychromatic OTFs is performed next for both correction states, through the superposition of the monochromatic ones stated in Eqs. (4.91) for uniform sampling of 36 wavelengths in the range between 400 and 700 nm. The x_λ, y_λ, and z_λ functions are set to be the spectral tristimulus values of the standard human observer CIE 1931, while the spectral power for the illumination corresponds to the standard illuminant C[49]. The results for system I, corresponding to a defocused plane, and for system II, at the image plane, are shown in Fig. 4.25. Note that in both cases the same RWD is used in the computation, as stated above.

4.3.3.3 Polychromatic Axial PSF

In this section we propose the use of a single two-dimensional RWD to compute the axial irradiance in image space provided by an imaging

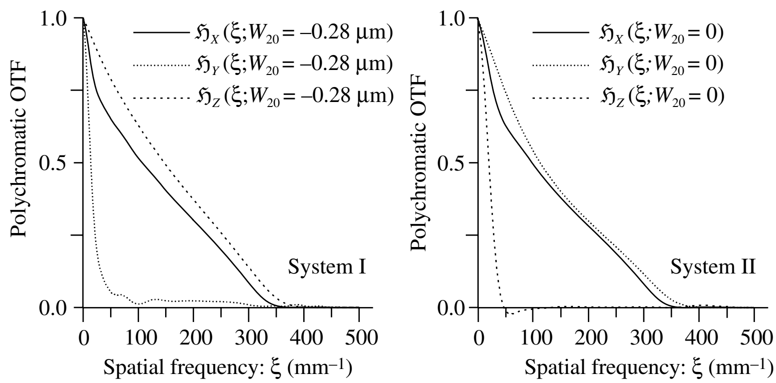

FIGURE 4.25 Polychromatic OTFs for (*a*) system I and (*b*) system II in Fig. 4.23, corresponding to a defocused plane ($W_{20} = -0.28\ \mu$m) and image plane, respectively.

system with polychromatic illumination. In fact, the proposed technique is a straightforward extension of what is stated in Sec. 4.3.1.1, namely, that the axial irradiance distribution $I(0, 0, z)$ provided by a system with an arbitrary value of SA can be obtained from the single RWT $RW_{q^{0,0}}(x, \xi)$ of the mapped pupil $q^{0,0}(s)$ in Eq. (4.75). When an object point source is used, this irradiance distribution corresponds, of course, to the on-axis values of the three-dimensional PSF of the imaging system. For notation convenience we denote $I_\lambda(z) = I(0, 0, z)$ in this section.

According to the discussion in Sec. 4.3.3.2, the account for chromaticity information leads to a proper generalization of the monochromatic irradiances to the polychromatic case through three functions, namely,

$$
\begin{aligned}
X(W_{20}) &= \int_\Lambda I_\lambda(z) S(\lambda) x_\lambda \, d\lambda \\
Y(W_{20}) &= \int_\Lambda I_\lambda(z) S(\lambda) x_\lambda \, d\lambda \\
Z(W_{20}) &= \int_\Lambda I_\lambda(z) S(\lambda) x_\lambda \, d\lambda
\end{aligned}
\tag{4.92}
$$

where $S(\lambda)$, $V(\lambda)$, x_λ, y_λ, and z_λ stand for the magnitudes used in the previous section. The defocus coefficient is defined in Eq. (4.51). However, it is often more useful to describe a chromatic signal through a combination of these basic functions. A conventional choice for these new parameters is the set

$$\begin{aligned} x(W_{20}) &= \frac{X(W_{20})}{X(W_{20}) + Y(W_{20}) + Z(W_{20})} \\ y(W_{20}) &= \frac{Y(W_{20})}{X(W_{20}) + Y(W_{20}) + Z(W_{20})} \end{aligned} \tag{4.93}$$

known as *chromaticity coordinates*, along with the parameter $Y(W_{20})$. If the sensitivity functions are selected to be the spectral tristimulus values of the human eye, the $Y(W_{20})$ parameter is known as illuminance and it is associated basically with the brightness of the chromatic stimulus. On the other hand, in this case the chromaticity coordinates provide a joint description for the hue and saturation of the colored signal.[49]

Anyway, as in the previous section, the evaluation of these magnitudes requires the computation of the monochromatic components for a sufficient number of spectral components. The use of conventional techniques, as stated earlier, is not very efficient at this stage, since the computation performed for a fixed axial point, a given wavelength, and a given aberration state cannot be applied to any other configuration. The method proposed in Sec. 4.3.1.1 represents a much more efficient solution since all the monochromatic values of the axial irradiance can be obtained, for different aberration correction states, from a single two-dimensional display associated with the pupil of the system.

To describe this proposal in greater detail, let us consider the system presented in Fig. 4.9 with $\alpha = 0$. According to the formulas in Sec. 4.3.1.1, the axial irradiance distribution in image space, for a given spectral component, can be expressed as

$$I_\lambda(z) = \frac{1}{\lambda^2 (f+z)^2} RW_{q^{0,0}}\left(x_\theta(z), \theta\right) \tag{4.94}$$

where $q^{0,0}(s)$ represents the zero-order circular harmonic of the pupil $Q(r_N, \phi)$, with $s = r_N^2 + \frac{1}{2}$. The normalized coordinates r_N and ϕ are implicitly defined in Eq. (4.49). The specific coordinates $(x_\theta(z), \theta)$ for the RWT are given by Eqs. (4.64) and (4.65). Note that for systems with longitudinal chromatic aberration, the defocus coefficient W_{20} is substituted for the wavelength-dependent coefficient in Eq. (4.90). Note that now the whole dependence of the axial irradiance on λ, W_{40}, and z is established through these coordinates if the function $Q(r_N, \phi)$ itself does not depend on wavelength. This is the case when all the aberrations of the system, apart from SA and longitudinal chromatic aberration, have a negligible chromatic dependence. This is a very usual situation in well-corrected systems, and in this case, every axial position, SA and chromatic aberration state, and wavelength can be studied from the same two-dimensional RWD.

Thus, providing that these kinds of systems are analyzed, the polychromatic description for the axial image irradiance can be assessed by the formulas

$$
\begin{aligned}
X(W_{20}) &= \int\limits_{\Lambda} \frac{RW_{q^{0,0}}(x_\theta(z), \theta)}{\lambda^2 (f+z)^2} S(\lambda) x_\lambda \, d\lambda \\
Y(W_{20}) &= \int\limits_{\Lambda} \frac{RW_{q^{0,0}}(x_\theta(z), \theta)}{\lambda^2 (f+z)^2} S(\lambda) y_\lambda \, d\lambda \qquad (4.95) \\
Z(W_{20}) &= \int\limits_{\Lambda} \frac{RW_{q^{0,0}}(x_\theta(z), \theta)}{\lambda^2 (f+z)^2} S(\lambda) z_\lambda \, d\lambda
\end{aligned}
$$

where the values of $(x_\theta(z), \theta)$ for every wavelength, axial position, and SA amount are given by Eqs. (4.64) and (4.65). Thus, once the RWD of the function $q^{0,0}(s)$ of the system is properly computed, these weighted superpositions can be quickly and easily calculated.[19,50,51]

As an example for testing this technique, we evaluate the axial response of a clear circular pupil imaging system, affected by spherical and longitudinal chromatic aberrations as shown in Fig. 4.26. Without loss of generality we assume here that the SA coefficient has a flat behavior for the considered spectral range. Once again, for the sake of simplicity, we assume that no other aberrations are present.

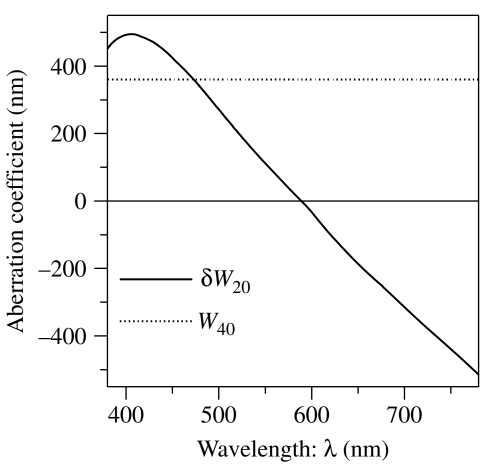

FIGURE 4.26 Aberration coefficients associated with the system under issue.

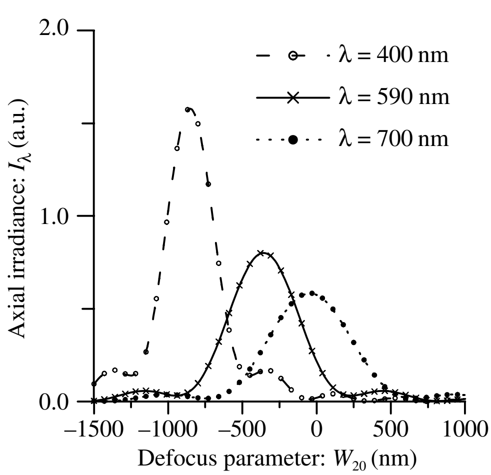

FIGURE 4.27 Axial irradiance values for the system under study. Solid lines represent the results by analytical calculation, while superimposed symbols correspond to the computation through the single RWD technique.

We consider 36 axial positions characterized by defocus coefficient values in a uniform sequence. We follow the same procedure as in earlier sections for the digital calculation of the RWD $RW_{q^{0,0}}(x_\theta, \theta)$. It is worth mentioning that for this pupil is possible to achieve an analytical result for the monochromatic axial behavior of the system for any value of W'_{20}, W_{40}, and λ, namely,[12]

$$I_\lambda(z) = \left[\frac{\pi a^2}{2\lambda f(f+z)}\right]^2 \frac{1}{W_{40}} \left| F\left[\frac{W'_{20}(\lambda) + 2W_{40}}{\sqrt{\lambda W_{40}}}\right] - F\left[\frac{W'_{20}(\lambda)}{\sqrt{\lambda W_{40}}}\right]\right|^2 \tag{4.96}$$

where

$$F(z) = \int_0^z \exp\left(\frac{i\pi t^2}{2}\right) dt \tag{4.97}$$

is the complex form of Fresnel integral. This analytical formula is used here to evaluate the results obtained by the proposed method. Figure 4.27 presents a comparison of these approaches for three different wavelengths in the visible spectral range. Excellent agreement can be observed in this figure.

Finally, we performed the calculation of the axial values for the chromaticity coordinates and the illuminance, by assuming the same

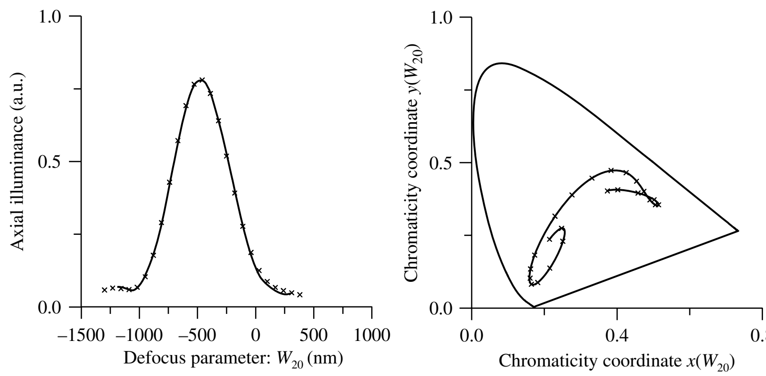

FIGURE 4.28 Axial illuminance and chromaticity coordinates for the system under study. Here solid lines represent the results obtained by the conventional method, while superimposed symbols correspond to the computation through the single RWD technique.

settings for the sensitivity functions and the illuminant as in the previous section. The values obtained with the method presented here are compared in Fig. 4.28 with the ones obtained by applying the same classic technique as in Sec. 4.3.3.2. Again, a very good agreement between them can be seen. A more detailed comparison of both methods is presented in Ref. 19.

4.4 Design of Imaging Systems and Optical Signal Processing by Means of RWT

4.4.1 Optimization of Optical Systems: Achromatic Design

We now present a design method for imaging systems working under polychromatic illumination on a RWT basis. In particular, we fix our attention on the optimal compensation of the axial chromatic dispersion of the Fresnel diffraction patterns of a plane object Although this proposal can be applied to a wide variety of systems, we concentrate on an optical system specially designed for this purpose. This device allows us to obtain the image of any arbitrary diffraction pattern with very low residual chromatic aberration.[52,53] The optical system, sketched in Fig. 4.29, works under planar broadband illumination. The only two optical elements in this device are an achromatic lens, with focal length f, and an on-axis kinoform zone plate. This element acts,

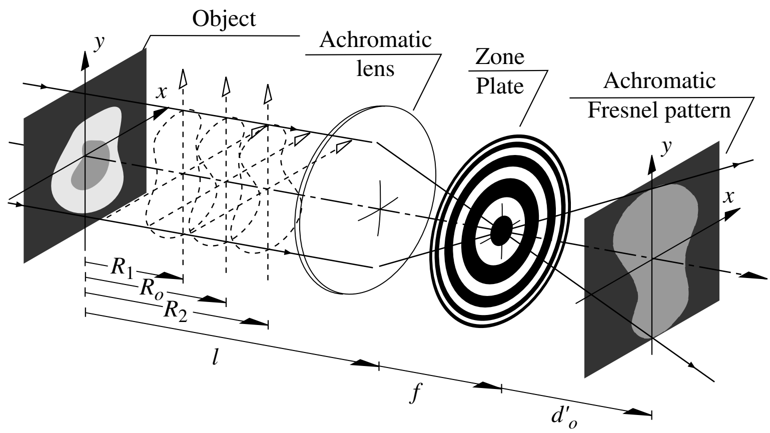

FIGURE 4.29 Achromatic imaging system under study.

from a scalar paraxial diffraction point of view, as a conventional thin lens with a focal length proportional to the inverse of the wavelength λ of the incoming light, i.e.,

$$Z(\lambda) = Z_o \frac{\lambda_o}{\lambda} \tag{4.98}$$

λ_o being a reference design wavelength and $Z_o = Z(\lambda_o)$. We note that although the effect of residual focuses can be significant for those wavelengths that are different from the design wavelength, we do not consider it here.

Our goal in this section is to achieve the optimal relationship between the geometric distances in the imaging system to obtain an output image corresponding to a given Fresnel pattern with minimum chromatic aberration. Thus, let us consider a given diffraction pattern located at a distance R_o from the object for the reference chromatic component of wavelength λ_o. It is well known that with parallel illumination the same diffraction pattern appears for any other spectral component at a distance from the input mask given by

$$R(\lambda) = R_o \frac{\lambda_o}{\lambda} \tag{4.99}$$

In this way, if the limits of the spectrum of the incoming radiation are λ_1 and λ_2, the same diffraction pattern is replicated along the optical axis between the planes characterized by distances $R_1 = R(\lambda_1)$ and $R_2 = R(\lambda_2)$, providing a *dispersion volume* for the diffraction pattern under study. However, if we fix our attention on the reference plane located at a distance R_o from the object, for $\lambda \neq \lambda_o$ we obtain a different structure for the diffracted pattern, and, therefore, the final superposition of all the spectral components of the incoming light produces a chromatic blur of the monochromatic result. To analyze this effect, we again use the RWT approach to describe the spectral components of this Fresnel pattern. Since the above dispersion volume is transformed, by means of the imaging system, into a different image volume, it is interesting to derive the geometric conditions that provide a minimum value for its axial elongation in the image space. Equivalently, the same RWT analysis will be performed at the output of the system to analyze the chromatic blur at the output plane for the reference wavelength λ_o.

For the sake of simplicity, we consider a one-dimensional amplitude transmittance $t(x)$ for the diffracting object. Let us now apply our approach to calculate the irradiance free-space diffraction pattern under issue through the RWT of the object mask. If we recall the result in Eq. (4.36) for $z = R_o$, we obtain that each spectral component of this Fresnel pattern is given by

$$I_o(x;\lambda) \propto RW_t\left(x_\theta(\lambda), \theta(\lambda)\right), \quad \tan\theta(\lambda) = -\lambda R_o,$$
$$x_\theta(\lambda) = \frac{x}{\lambda R_o}\sin\theta(\lambda) \tag{4.100}$$

In this equation the chromatic blur is considered through the spectral variation of the coordinates in the RWT for any given transverse position x in the diffraction pattern. Thus, for a fixed observation position there is a region in the Radon space that contains all the points needed to compute the polychromatic irradiance. If we define $\theta_i = \arctan(\lambda_i R_o)$, for $i = 1, 2$, the width of this region in both Radon-space directions can be estimated as

$$\Delta\theta = |\theta_1 - \theta_2|, \qquad \Delta x_\theta = \left|\frac{x}{R_o}\left(\frac{\sin\theta_1}{\lambda_1} - \frac{\sin\theta_2}{\lambda_2}\right)\right| \tag{4.101}$$

Note that the smaller this region is, the less is the effect of the chromatic blur affecting the irradiance at the specified observation point. To achieve an *achromatization* of the selected diffraction pattern, this region has to be reduced in the output plane of the optical setup.

Let us now fix our attention on the effect of the imaging system on the polychromatic diffraction pattern under issue. Again, we use the RWT approach to achieve this description by simply noting that the system behaves as an *abcd* device that links the object plane and the selected output plane. The transformation matrix M_{achr} can be obtained as a sequence of elemental transformations (see Fig. 4.29), namely, free propagation at a distance l, propagation through the achromatic lens, free propagation to the focal plane of that element, passage through the zone plate, and, finally free propagation at a distance d_o'. The output plane is selected as the image plane of the diffraction pattern under study for $\lambda = \lambda_o$. Thus, by using the results in Sec. 4.2.1, it is straightforward to obtain

$$M(\lambda) = \begin{pmatrix} 1 - \dfrac{l}{f} - \dfrac{f}{Z(\lambda)} & -\lambda \left(f - m_o f + m_o l + \dfrac{f^2 m_o}{Z(\lambda)} \right) \\ \dfrac{1}{\lambda f} & m_o \end{pmatrix} \tag{4.102}$$

where the following restriction applies to the fixed desired output plane

$$l = R_o + f - \frac{f}{m_o} - \frac{f^2}{Z_o} \tag{4.103}$$

where $m_o = -d'_o/f$ is the magnification obtained at the fixed image plane (for $\lambda = \lambda_o$). The relationship between the RWTs of the input object and the output Fresnel pattern for each spectral channel now can be established by application of Eqs. (4.27) and (4.28). In particular, by setting $\theta = 0$ we find

$$I'_o(x; \lambda) \propto RW_t \left(x_{\theta'}(\lambda), \theta'(\lambda) \right)$$
$$\tan\theta'(\lambda) = \lambda \left[R_o + \frac{f^2}{Z_o} \left(\frac{\lambda}{\lambda_o} - 1 \right) \right], \qquad x_{\theta'} = \frac{x}{m_o} \cos\theta'(\lambda) \tag{4.104}$$

Therefore, for the polychromatic description of the output diffraction pattern we have to sum values of the RWT of the transmittance of the object in a region in the Radon domain whose size in both dimensions is given by

$$\Delta\theta' = |\theta'_{\max} - \theta'_{\min}|, \qquad \Delta x_{\theta'} = \left| \frac{x}{m_o} (\cos\theta_{\max} - \cos\theta_{\min}) \right| \tag{4.105}$$

where

$$\theta'_{\max} = \max\{\theta'(\lambda) | \lambda \in [\lambda_1, \lambda_2]\}, \qquad \theta'_{\min} = \min\{\theta'(\lambda) | \lambda \in [\lambda_1, \lambda_2]\} \tag{4.106}$$

The specific values of these limits, which define the extension of the integration region in Radon space in the polychromatic case, depend on the particular values of the geometric design parameters f and Z_o of the imaging system. We now try to find a case that minimizes the chromatic blur in the output pattern. It is worth mentioning that exact achromatization of the pattern is achieved only when $\theta'(\lambda) = \theta'(\lambda_o)\ \forall\lambda \in [\lambda_1, \lambda_2]$, which cannot be fulfilled in practice, as can be seen from Eq. (4.104). However, a first-order approximation to that ideal correction can be achieved by imposing a stationary behavior for $\theta'(\lambda)$ around $\lambda = \lambda_o$. Mathematically, we impose

$$\left. \frac{d\theta'(\lambda)}{d\lambda} \right|_{\lambda_o} = 0 \tag{4.107}$$

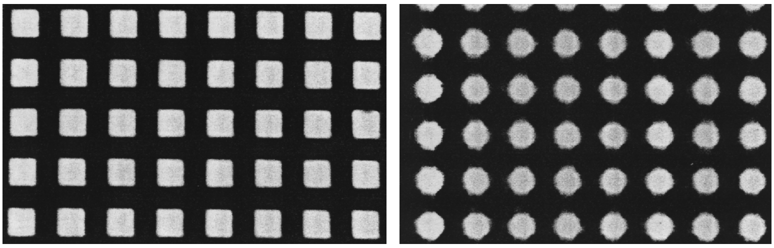

(*a*) (*b*)

FIGURE 4.30 Gray-scale display of the irradiance distribution to be achromatized: (*a*) Monochromatic pattern for $\lambda_o = 546.1$ nm. (*b*) Broadband (Hg lamp) irradiance distribution.

or, equivalently,

$$\left.\frac{d \tan \theta'(\lambda)}{d\lambda}\right|_{\lambda_o} = 0 \tag{4.108}$$

which leads to the optimal constraint

$$R_o = -\frac{f^2}{Z_o} \tag{4.109}$$

This condition transforms Eq. (4.103) into

$$l = 2R_o + f - \frac{f}{m_o} \tag{4.110}$$

Thus, the choice of a set of geometric parameters l, f, Z_o, and d'_o fulfilling the two above equations provides a design prescription for a first-order compensation of the chromatic blur in the diffraction pattern located, for $\lambda = \lambda_o$, at distance R_o from the object.[54]

To illustrate this design procedure and to check the predicted results, we present an experimental verification by using a two-dimensional periodic transmittance as an object, with the same period $p = 0.179$ mm in both orthogonal directions. As a Fresnel pattern to be achromatized, a self-imaging distribution is selected. In particular, after parallel illumination with $\lambda_o = 546.1$ nm, the distance $R_o = 11.73$ cm is selected. Figure 4.30*a* shows a picture of the irradiance distribution in that situation. In Fig. 4.30*b*, the irradiance distribution over the same plane, but when a polychromatic collimated beam from a high-pressure Hg lamp is used, is presented. The chromatic blur is clearly seen by comparing these two figures.

To optimally achromatize this diffraction pattern, we follow the prescriptions given in the above paragraphs. We use a kinoform lens

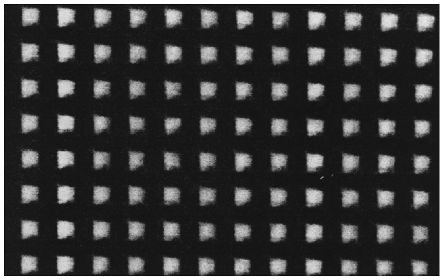

FIGURE 4.31 Gray-scale display of the achromatized irradiance distribution.

with $Z_o = -12$ cm, and we choose a value $d_o' = 10.00$ cm. Therefore, we select a focal distance for the achromatic lens $f = \sqrt{-Z_o R_o} = 11.86$ cm, and we place that object at a distance $l = 2R_o + f + f^2/d_o' = 49.39$ cm from that lens. A gray-scale display of the output irradiance is presented in Fig. 4.31. The comparison between this result and the monochromatic one in Fig. 4.30*a* shows the high achromatization level obtained with the optimized system.

4.4.2 Controlling the Axial Response: Synthesis of Pupil Masks by RWT Inversion

In Sec. 4.3.1.1 we showed that the axial behavior of the irradiance distribution provided by a system with an arbitrary value of SA can be obtained from the single RWT of the mapped pupil $q^{0,0}(s)$ of the system. In fact, Eq. (4.74) can be considered the keystone of a pupil design method[55] in which the synthesis procedure starts by performing a tomographic reconstruction of $W_{q^{0,0}}(x, \xi)$ from the projected function $I(0, 0, z)$ representing the irradiance at the axial points—variable W_{20}—for a sufficient set of values of W_{40}. Thus, the entire two-dimensional Wigner space can be sampled on a set of lines defined by these parameters. The backprojection algorithm converts the desired axial irradiance for a fixed value of W_{40}, represented by a one-dimensional function, to a two-dimensional function by smearing it uniformly along the original projection direction (see Fig. 4.8). Then the algorithm calculates the summation function that results when all backprojections are summed over all projection angles θ, i.e., for all the different values of W_{40}. The final reconstructed function $W_{q^{0,0}}(x, \xi)$ is obtained by a proper filtering of the summation image.[55] Once the WDF is synthesized with the values of the input axial irradiances, the pupil function is obtained by use of Eq. (4.4). Finally, the geometric mapping in Eq. (4.57) is inverted to provide the desired pupil function.

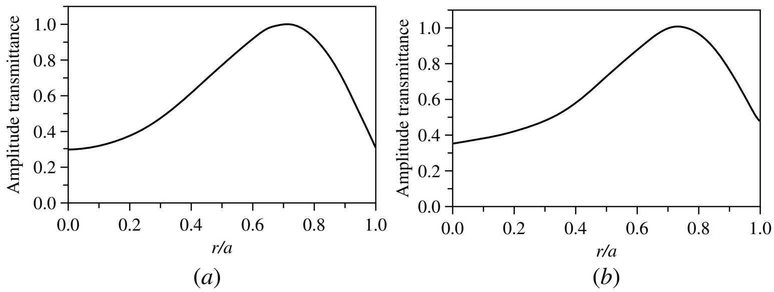

FIGURE 4.32 (*a*) Amplitude transmittance of a desired pupil function. (*b*) Phase-space tomographic reconstruction of the same pupil.

To illustrate the method, we numerically simulated the synthesis of an annular apodizer represented in Fig. 4.32. It has been shown that its main features are to increase the focal depth and to reduce the influence of SA. From this function we numerically determined first the $W_{q^{0,0}}(x, \xi)$ function, using the WDF definition, and thereby the projected distributions defined by the RWT, obtaining the axial irradiance distribution for different values of SA. In this case, we used 1024 values for both W_{40}/λ and W_{20}/λ, ranging from -16 to $+16$. We treated these distributions as if they represented the desired axial behavior for a variable SA, and we reconstructed the WDF by using a standard filtered backprojection algorithm for the inverse Radon transform. From the reconstructed WDF we obtained the synthesized pupil function $p(\vec{x})$ by performing the discrete one-dimensional inverse FT of $W_{q^{0,0}}(x, \xi)$. The result is shown in Fig. 4.32*b*. As can be seen, the amplitude transmittance of the synthesized pupil function closely resembles the original apodizer in Fig. 4.32*a*.

4.4.3 Signal Processing through RWT

Throughout this chapter we have discussed the RWT as a mathematical tool that allows us to develop novel and interesting applications in optics. Among several mathematical operations that can be optically implemented, correlation is one of the most important because it can be used for different applications, such as pattern recognition and object localization. Optical correlation can be performed in coherent systems by use of the fact that the counterpart of this operation in the Fourier domain is simply the product of both signals. To implement this operation, several optical architectures were developed, such as the classic VanderLugt and joint transform correlators.[56,57] Because conventional correlation is a shift-invariant operation, the correlation output simply moves if the object translates at the input plane. In many cases this property is necessary, but there are situations in which the position of the object provides additional information such as in image coding or cryptographic applications, and so shift invariance is a disadvantage.

The fractional correlation[58,59] is a generalization of the classic correlation that employs the optical FrFT of a given fractional order p instead of the conventional FT. Conventionally, the fractional correlation is obtained as the inverse Fourier transform of the product of the FrFT of both the reference and the input objects, but for a single fractional order p at a time. The fractional order involved in the FrFT controls the amount of shift variance of the correlation. As is well known, the shift-variance property modifies the intensity of the correlation output when the input is shifted. In several pattern recognition applications this feature is useful, for example, when an object should be recognized in a relevant area and rejected otherwise, or when the recognition should be based on certain pixels in systems with variable spatial resolution. However, the optimum amount of variance for a specific application is frequently difficult to predict, and therefore more complete information would certainly be attained from a display showing several fractional correlations at the same time. Ideally, such a display should include the classic shift-invariant correlation as the limiting case. In this section we will show that such a multichannel fractional correlator could be easily implemented from the RWD system presented in Sec. 4.2.2. The resulting optical system generates a simultaneous display of fractional correlations of a one-dimensional input for a continuous set of fractional orders in the range $p \in [0, 1]$.

We start by recalling[58] the definition of the fractional correlation between two one-dimensional functions $f(x)$ and $f'(x)$

$$C_p(x) = \mathcal{F}^{-1}\{F_p(\alpha)F'^{*}_p(\alpha), x\} \tag{4.111}$$

It is important to note that with the above definition the classic correlation is obtained if we set $p = 1$. The product inside the brackets of Eq. (4.111) can be optically achieved simultaneously for all fractional orders, ranging between $p = 0$ and $p = 1$, following a two-step process. In the first stage, the RWD of the input is obtained with the experimental configuration shown in Sec. 4.2.2. A matched filter can be obtained at the output plane if, instead of recording the intensity, we register a hologram of the field distribution at this plane with a reference wavefront at an angle θ. (see Fig. 4.33).

In the second stage, the obtained multichannel matched filter is located at the filter plane, and the input function to be correlated is located at the input plane (see Fig. 4.34).

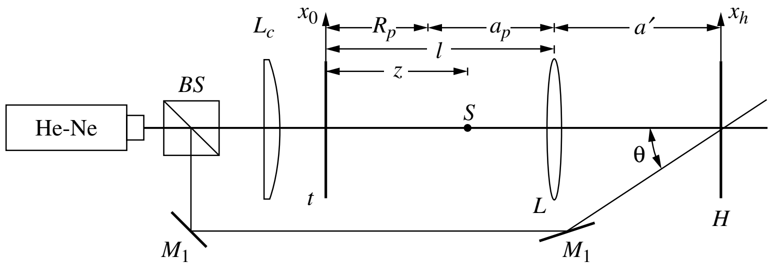

FIGURE 4.33 Multichannel matched filter registration for a fractional correlation. The elements are the same as in Sec. 4.2.2, except for BS (beam splitter) and $M1$ and $M2$ (plane mirrors).

Because the transmittance of the holographic filter has one term proportional to the complex conjugate of the reference field in Eq. (4.111), for each fractional order channel the field immediately behind the filter plane has one term proportional to the product of the complex conjugate of the FrFT of the reference function $f'(x)$ and the same FrFT of the input function $f(x)$. Thus the multiplicative phase factor in this equation and the corresponding one of the matched filter cancel out. Besides, although the experimental FrFT for a given order p is approximated owing to the scale error discussed in Sec. 4.2.2, the experimental fractional correlation can be obtained exactly because this error affects both $F_p(\alpha)$ and $F_p'^*(\alpha)$. Finally, the diffracted field at angle θ is collected by the lens L_c, which performs a one-dimensional FT. Because each fractional order $p \in [0, 1]$ has an independent one-dimensional correlation channel, all the fractional correlations for this

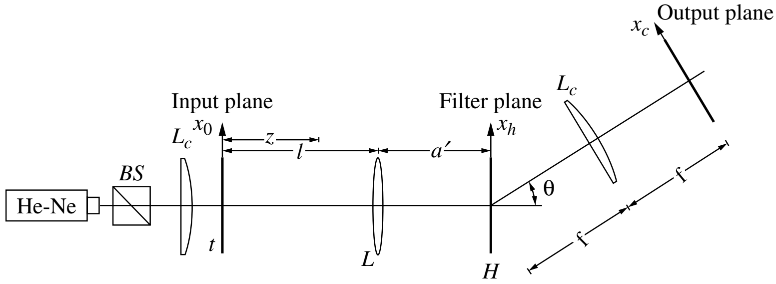

FIGURE 4.34 Multichannel fractional correlator. The filter H corresponds to the one obtained in the setup of Fig. 4.33.

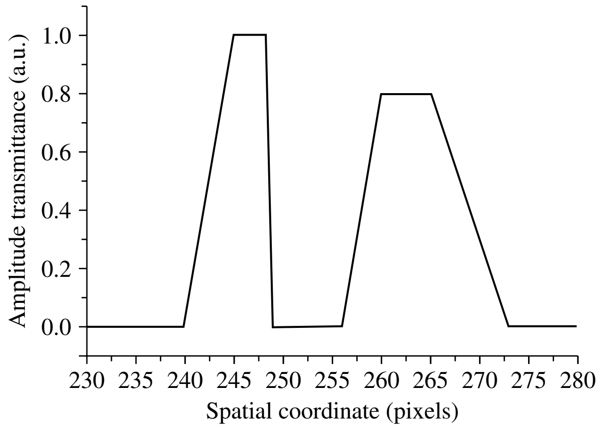

FIGURE 4.35 Amplitude transmittance of an input object selected to perform multichannel fractional correlation.

range of fractional orders are obtained simultaneously at the output plane. Thus a two-dimensional display is obtained in which the fractional correlations are ordered in a continuous display along the axis normal to the plane shown in Fig. 4.34.

The shift-variant property of the FrFT correlation was confirmed experimentally in Ref. 60. Here we present a numerical simulation using an input object whose amplitude transmittance is shown in Fig. 4.35. It represents a double nonsymmetric slit with a continuous gray-level amplitude transmittance. The continuous transition between the shift-variant case $p = 0$ and the shift-invariant case $p = 1$ is confirmed in Fig. 4.36. In this figure the fractional autocorrelation of the input is considered, but the reference objects are shifted at the input plane.

Figure 4.36*a* shows the fractional correlations when the input is shifted an amount of one-half of the object size, and Fig. 4.36*b* shows the fractional correlation when the input is shifted an amount equal to the size of the object. The variant behavior of the fractional correlation can be clearly seen by the comparison of these figures. Both displays coincide near to $p = 1$ (except for the location of the maxima), but for lower values of p the fractional correlation is highly dependent on the magnitude of the shift. As can be seen in the three-dimensional plot in this figure, for a fixed displacement the correlation peak increases with p. As expected for $p = 1$, the correlation peak is the classic one located at the input position. For values ranging between $p = 0.5$ and $p = 1$, the correlation peak did not change appreciably. The

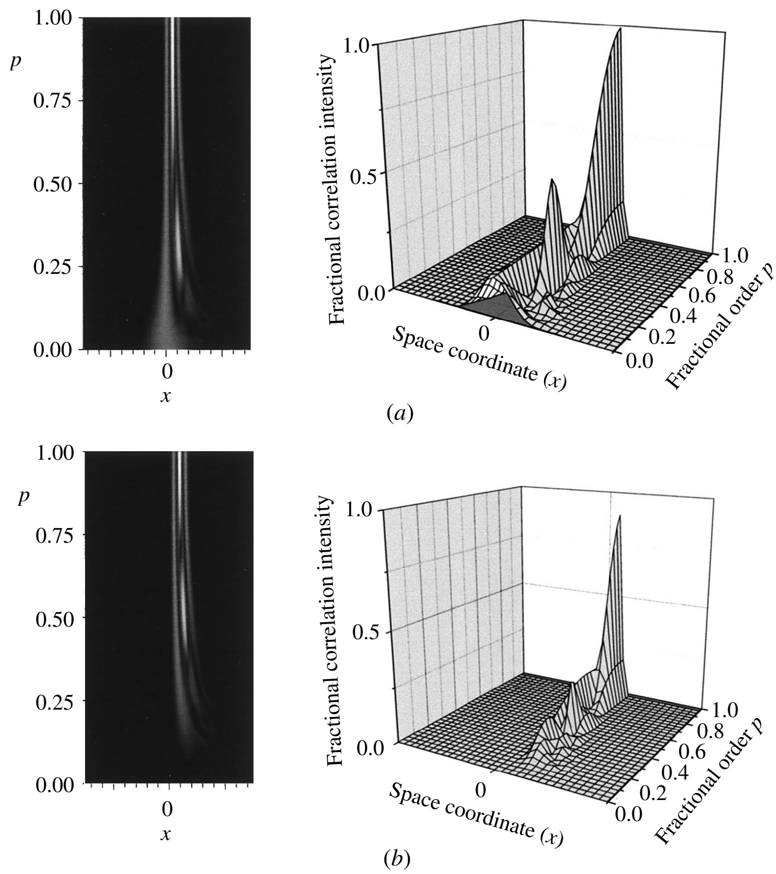

FIGURE 4.36 Multichannel fractional autocorrelation of the function represented in Fig. 4.35 with (*a*) a shift in the input plane of one-half of the object size and (*b*) a shift of the whole size of the object.

shift-variant property becomes evident for values close to $p = 0.25$. It can be seen that as the fractional order becomes lower, the peak degenerates and shifts disproportionately toward the object position. Thus, the output of the system shows a variable degree of space variance ranging from the pure shift variance case $p = 0$ to the pure shift invariance case $p = 1$, that is, the classic correlation. This kind of representation provides information about the object, such as classic correlation, but also quantifies its departure from a given reference position.

Acknowledgments

The authors would like to express their gratitude to P. Andrés, S. Granieri, E. Sicre, and E. Silvestre for their contributions in the research revisited in this chapter. They also acknowledge financial support of Ministerio de Ciencia y Tecnología, Spain (Grants DPI 2006-8309 and DPI 2008-02953).

References

1. J. C. Wood and D. T. Barry, "Radon transformation of time-frequency distributions for analysis of multicomponent signals," *Proc. Int. Conf. Acoust. Speech Signal Process.* **4**: 257–261 (1992).
2. J. C. Wood and D. T. Barry, "Linear signal synthesis using the Radon-Wigner transform," *IEEE Trans. Signal Process.* **42**: 2105–2111 (1994).
3. L. Cohen, *Time-Frequency Analysis*, Prentice-Hall, Upper Saddle River, N.J., 1995.
4. D. Mendlovic, R. G. Dorsch, A. W. Lohmann, Z. Zalevsky, and C. Ferreira, "Optical illustration of a varied fractional Fourier-transform order and the Radon-Wigner display," *Appl. Opt.* **35**: 3925–3929 (1996).
5. A. W. Lohmann, "Image rotation, Wigner rotation, and the fractional Fourier transform," *J. Opt. Soc. Am.* **A10**: 2181–2186 (1993).
6. S. Granieri, W. D. Furlan, G. Saavedra, and P. Andrés, "Radon-Wigner display: A compact optical implementation with a single varifocal lens," *Appl. Opt.* **36**: 8363–8369 (1997).
7. P. Pellat-Finet, "Fresnel diffraction and the fractional-order Fourier transform," *Opt. Lett.* **19**: 1388–1390 (1994).
8. P. Andrés, W. D. Furlan, G. Saavedra, and A. W. Lohmann, "Variable fractional Fourier processor: A simple implementation," *J. Opt. Soc. Am.* **A14**: 853–858 (1997).
9. E. Tajahuerce, G. Saavedra, W. D. Furlan, E. E. Sicre, and P. Andrés, "White-light optical implementation of the fractional fourier transform with adjustable order control," *Appl. Opt.* **39**: 238–245 (2000).
10. Y. Zhang, B. Gu, B. Dong, and G. Yang, "Optical implementations of the Radon-Wigner display for one-dimensional signals," *Opt. Lett.* **23**: 1126–1128 (1998).
11. Y. Zhang, B.-Y. Gu, B.-Z. Dong, and G.-Z. Yang, "New optical configurations for implementing Radon-Wigner display: Matrix analysis approach," *Opt. Comm.* **160**: 292–300 (1999).
12. H. H. Hopkins and M. J. Yzuel, "The computation of diffraction patterns in the presence of aberrations," *Optica Acta* **17**: 157–182 (1970).
13. M. J. Yzuel and F. Calvo, "Point-spread function calculation for optical systems with residual aberrations and non-uniform transmission pupil," *Optica Acta* **30**: 233–242 (1983).
14. J. J. Stamnes, B. Spjelkavik, and H. M. Pedersen, "Evaluation of diffraction integrals using local phase and amplitude approximations," *Optica Acta* **30**: 207–222 (1983).
15. H. G. Kraus, "Finite element area and line integral transforms for generalization of aperture function and geometry in Kirchhoff scalar diffraction theory," *Opt. Eng.* **32**: 368–383 (1993).
16. L. A. D'Arcio, J. J. M. Braat, and H. J. Frankena, "Numerical evaluation of diffraction integrals for apertures of complicated shape," *J. Opt. Soc. Am.* **A11**: 2664–2674 (1994).
17. G. Saavedra, W. D. Furlan, E. Silvestre, and E. Sicre, "Analysis of the irradiance along different paths in the image space using the Wigner distribution function," *Opt. Comm.* **139**: 11–16 (1997).

18. W. D. Furlan, G. Saavedra, E. Silvestre, and M. Martínez-Corral, "On-axis irradiance for spherically aberrated optical systems with obscured rectangular apertures: A study using the Wigner distribution function," *J. Mod. Opt.* **45**: 69–77 (1998).
19. W. D. Furlan, G. Saavedra, E. Silvestre, J. A. Monsoriu, and J. D. Patrignani, "Assessment of a Wigner-distribution-function-based method to compute the polychromatic axial response given by an aberrated optical system," *Opt. Eng.* **42**: 753–758 (2003).
20. W. D. Furlan, G. Saavedra, J. A. Monsoriu, and J. D. Patrignani, "Axial behaviour of Cantor ring diffractals," *J. Opt. A: Pure Appl. Opt.* **5**: S361–S364 (2003).
21. W. D. Furlan, M. Martínez-Corral, B. Javidi, and G. Saavedra, "Analysis of 3-D integral imaging displays using the Wigner distribution," *J. Disp. Technol.* **2**: 180–185 (2006).
22. P. Andrés, M. Martínez-Corral, and J. Ojeda-Castañeda, "Off-axis focal shift for rotationally nonsymmetric screens," *Opt. Lett.* **18**: 1290–1292 (1993).
23. A. Dubra and J. A. Ferrari, "Diffracted field by an arbitrary aperture," *Am. J. Phys.* **61**: 87–92 (1999).
24. W. D. Furlan, G. Saavedra, and S Granieri, "Simultaneous display of all the Fresnel diffraction patterns of one-dimensional apertures," *Am. J. Phys.* **69**: 799 (2001).
25. C. Allain and M. Cloitre, "Optical diffraction on fractals," *Phys. Rev.* **B33**: 3566–3569 (1986).
26. Y. Sakurada, J. Uozumi, and T. Asakura, "Fresnel diffraction by one-dimensional regular fractals," *Pure Appl. Opt.* **1**: 29–40 (1992).
27. T. Alieva and F. Agulló-López, "Optical wave propagation of fractal fields," *Opt. Comm.* **125**: 267–274 (1996).
28. O. Trabocchi, S. Granieri, and W. D. Furlan, "Optical propagation of fractal fields: Experimental analysis in a single display," *J. Mod. Opt.* **48**: 1247–1253 (2001).
29. M. G. Raymer, M. Beck, and D. F. McAlister, "Complex wave-field reconstruction using phase-space tomography," *Phys. Rev. Lett.* **72**: 1137–1140 (1994).
30. D. F. McAlister, M. Beck, L. Clarke, A. Mayer, and M. G. Raymer, "Optical phase retrieval by phase-space tomography and fractional-order Fourier transforms," *Opt. Lett.* **20**: 1181–1183 (1994).
31. Y. Li, G. Eichmann, and M. Conner, "Optical Wigner distribution and ambiguity function for complex signals and images," *Opt. Comm.* **67**: 177–179 (1988).
32. G. Shabtay, D. Mendlovic, and Z. Zalevsky, "Proposal for optical implementation of the Wigner distribution function," *Appl. Opt.* **37**: 2142–2144 (1998).
33. R. L. Easton, Jr., A. J. Ticknor, and H. H. Barrett, "Application of the Radon transform to optical production of the Wigner distribution," *Opt. Eng.* **23**: 738–744 (1984).
34. W. D. Furlan, C. Soriano, and G. Saavedra, "Opto-digital tomographic reconstruction of the Wigner distribution function of complex fields," *Appl. Opt.* **47**: E63–E67 (2008).
35. A. C. Kak and M. Slaney, *Principles of Computerized Tomographic Imaging*, IEEE Press, New York, 1988.
36. U. Gopinathan, G. Situ, T. J. Naughton, and J. T. Sheridan, "Noninterferometric phase retrieval using a fractional Fourier system," *J. Opt. Soc. Am.* **A25**: 108–115 (2008).
37. M. Born and E. Wolf, *Principles of Optics: Electromagnetic Theory of Propagation, Interference and Diffraction of Light*, (7th ed., Cambridge University Press, Cambridge, 1999, Chap. 9.
38. H. H. Hopkins, "The aberration permissible in optical systems," *Proc. Phys. Soc.* **B70**: 449–470 (1957).
39. H. Bartelt, J. Ojeda-Castañeda, and E. E. Sicre, "Misfocus tolerance seen by simple inspection of the ambiguity function," *Appl. Opt.* **23**: 2693–2696 (1984).

40. W. D. Furlan, G. Saavedra, and J. Lancis, "Phase-space representations as a tool for the evaluation of the polychromatic OTF," *Opt. Comm.* **96**: 208–213 (1993).
41. W. D. Furlan, M. Martínez-Corral, B. Javidi, and G. Saavedra, "Analysis of 3-D integral imaging display using the Wigner distribution," *J. Disp. Technol.* **2**: 180–185 (2006).
42. K. H. Brenner , A. W. Lohmann, and J. Ojeda-Castañeda, "The ambiguity function as a polar display of the OTF," *Opt. Comm.* **44**: 323 (1983).
43. W. D. Furlan, G. Saavedra, and J. Lancis, "Phase-space representations as a tool for the evaluation of the polychromatic OTF," *Opt. Comm.* **96**: 208–213 (1993).
44. J. Bescós and J. Santamaría, "Formation of color images: Optical transfer functions for the tristimulus values," *Photogr. Sci. and Eng.* **21**: 355–362 (1977).
45. J. Bescós, J. H. Altamirano, A. Santisteban, and J. Santamaría, "Digital restoration models for color imaging," *Appl. Opt.* **27**: 419–424 (1988).
46. R. Barnden, "Calculation of axial polychromatic optical transfer function," *Optica Acta* **21**: 981–1003 (1974).
47. R. Barnden, "Extra-axial polychromatic optical transfer function," *Optica Acta* **23**: 1–24 (1976).
48. M. Takeda, "Chromatic aberration matching of the polychromatic optical transfer function," *Appl. Opt.* **20**: 684–687 (1981).
49. G. Wyszecki and W. S. Stiles, *Color Science*, Wiley, New York, 1982).
50. W. D. Furlan, G. Saavedra, E. Silvestre, M. J. Yzuel, and P. Andrés, "Polychromatic merit functions in terms of the Wigner distribution function," *Proc. SPIE* **2730**: 252–255 (1996).
51. W. D. Furlan, G. Saavedra, E. Silvestre, P. Andrés, and M. J. Yzuel, "Polychromatic axial behavior of aberrated optical systems: Wigner distribution function approach," *Appl. Opt.* **36**: 9146–9151 (1997).
52. P. Andrés, J. Lancis, E. E. Sicre, and E. Bonet, "Achromatic Fresnel diffraction patterns," *Opt. Comm.* **104**: 39–45 (1993).
53. P. Andrés, J. Lancis, E. Tajahuerce, V. Climent, and G. Saavedra, "White-light optical information processing with achromatic processors," *1994 OSA Tech. Digest Series* **11**: 220–223 (1994).
54. J. Lancis, E. E. Sicre, E. Tajahuerce, and P. Andrés, "White-light implementation of the Wigner-distribution function with an achromatic processor," *Appl. Opt.* **34**: 8209–8212 (1995).
55. W. Furlan, D. Zalvidea, and G. Saavedra, "Synthesis of filters for specified axial irradiance by use of phase-space tomography," *Opt. Comm.* **189**: 15–19 (2001).
56. A. Vander Lugt, *Optical Signal Processing*, Wiley, New York, 1992.
57. J. W. Goodman, *Introduction to Fourier Optics*, McGraw Hill, New York, 1996.
58. D. Mendlovic, H. M. Ozaktas, and A. W. Lohmann, "Fractional correlation," *Appl. Opt.* **34**: 303–309 (1995).
59. S. Granieri, R. Arizaga, and E. E. Sicre, "Optical correlation based on the fractional Fourier transform," *Appl. Opt.* **36**, 6636–6645 (1997).
60. S. Granieri, M. Tebaldi, and W. D. Furlan, "Parallel fractional correlation: An optical implementation," *Appl. Opt.* **40**: 6439–6444 (2001).